5-2023

Nuclear and Cytoplasmic Spatial Protein Quality Control is Coordinated by Nuclear–Vacuolar Junctions and Perinuclear ESCRT

Emily M. Sontag
Marquette University, emily.sontag@marquette.edu

Fabián Morales-Polanco
Stanford University

Jian-Hua Chen
University of California, San Francisco

Gerry McDermott
University of California, San Francisco

Patrick T. Dolan
Stanford University

See next page for additional authors

Nature Cell Biology, Vol. 25 (2023): 699-713. DOI.

Nuclear and Cytoplasmic Spatial Protein Quality Control is Coordinated by Nuclear-Vacuolar Junctions and Perinuclear ESCRT

Emily M. Sontag
Department of Biological Sciences, Marquette University, Milwaukee, WI, USA
Department of Biology, Stanford University, Stanford, CA, USA
Fabián Morales-Polanco
Department of Biology, Stanford University, Stanford, CA, USA
Jian-Hua Chen
Department of Anatomy, School of Medicine, University of California San Francisco, San Francisco, CA, USA
Gerry McDermott
Department of Anatomy, School of Medicine, University of California San Francisco, San Francisco, CA, USA
Patrick T. Dolan
Quantitative Virology and Evolution Unit, National Institute of Allergy and Infectious Diseases, Bethesda, MD, USA
Department of Biology, Stanford University, Stanford, CA, USA

Daniel Gestaut
Department of Biology, Stanford University, Stanford, CA, USA
Mark A. Le Gros
Department of Anatomy, School of Medicine, University of California San Francisco, San Francisco, CA, USA
Molecular Biophysics and Integrated Bioimaging Division, Lawrence Berkeley National Laboratory, Berkeley, CA, USA
Carolyn Larabell
Department of Anatomy, School of Medicine, University of California San Francisco, San Francisco, CA, USA
Molecular Biophysics and Integrated Bioimaging Division, Lawrence Berkeley National Laboratory, Berkeley, CA, USA
Judith Frydman
Department of Biology, Stanford University, Stanford, CA, USA

Abstract

Effective protein quality control (PQC), essential for cellular health, relies on spatial sequestration of misfolded proteins into defined inclusions. Here we reveal the coordination of nuclear and cytoplasmic spatial PQC. Cytoplasmic misfolded proteins concentrate in a cytoplasmic juxtanuclear quality control compartment, while nuclear misfolded proteins sequester into an intranuclear quality control compartment (INQ). Particle tracking reveals that INQ and the juxtanuclear quality control compartment converge to face each other across the nuclear envelope at a site proximal to the nuclear–vacuolar junction marked by perinuclear ESCRT-II/III protein Chm7. Strikingly, convergence at nuclear–vacuolar junction contacts facilitates VPS4-dependent vacuolar clearance of misfolded cytoplasmic and nuclear proteins, the latter entailing extrusion of nuclear INQ into the vacuole. Finding that nuclear–vacuolar contact sites are cellular hubs of spatial PQC to facilitate vacuolar clearance of nuclear and cytoplasmic inclusions highlights the role of cellular architecture in proteostasis maintenance.

Main

Misfolded proteins can acquire toxic conformations, disrupting essential cellular processes[1,2,3,4,5,6] and leading to human diseases ranging from neurodegeneration to cancer[7,8,9,10]. To prevent this, cellular proteostasis is maintained by a network of chaperones and clearance factors promoting protein quality control (PQC)[11,12,13,14,15]. One fundamental PQC strategy is to spatially sequester misfolded proteins into distinctly localized membrane-less compartments. PQC compartments segregate and concentrate damaging conformers, enhancing their refolding or clearance through either the ubiquitin–proteasome system (UPS) or endo-lysosomal pathways[11,16,17,18]. Misfolded cytoplasmic proteins partition into distinct inclusions depending on their aggregation state. Insoluble amyloid proteins are sequestered into the Insoluble Protein Deposit (herein IPOD)[4,11,19]. Soluble misfolded proteins are sequestered into small, dynamic, endoplasmic reticulum (ER)-associated structures called Q-bodies[17], which, during sustained stress, coalesce along the endomembrane system[20] into a juxtanuclear quality control compartment (herein the JUNQ). Spatial PQC of cytoplasmic proteins through the IPOD and JUNQ pathways is evolutionarily conserved from yeast to mammalian cells[11,19]. In the nucleus, misfolded proteins are sequestered in a membrane-less intranuclear quality control compartment (herein INQ), proximal to the nucleolus[18,21,22].

In this Article, we examined the relationship between cytoplasmic and nuclear spatial PQC. Many studies showed cytoplasmic misfolded proteins being concentrated into the cytoplasmic JUNQ and cleared through an ER-anchored cytoplasmic UPS pathway[11,19,23,24]. It has also been proposed that clearance of cytoplasmic misfolded proteins requires import into the nucleus, whereby the JUNQ would form an inclusion identical to the INQ[18]. Addressing this issue, we unequivocally demonstrate that the JUNQ is cytoplasmic and the INQ is nuclear. Formation of these PQC compartments is coordinated to localize to opposite sides of the nuclear envelope, at a site marked by perinuclear ESCRT Chm7 and proximal to nuclear–vacuolar junctions (NVJs). Localization to the NVJ facilitates VPS4-dependent extrusion of the INQ into the vacuole, providing an alternative avenue for vacuolar clearance of nuclear misfolded proteins.

Nuclear and cytoplasmic spatial PQC is organelle specific

We used a set of validated nuclear and cytoplasmic spatial PQC substrates that are degraded upon misfolding and are stabilized in the presence of proteasomal inhibitors MG132 or bortezomib (Bz)[25] (Extended Data Fig. 1a and ref. [25]). A temperature-sensitive variant of Firefly Luciferase (herein LuciTs) that misfolds at 37 °C, and constitutively unfolded Von Hippel-Lindau (VHL) tumour suppressor[26,27] were restricted to either nucleus or cytoplasm by inclusion of a nuclear localization signal (NLS) or a nuclear export signal (NES), respectively (Fig. 1a). The PQC substrates were induced by growth in galactose at 25 °C, and then repressed by glucose exchange, which allows measuring their kinetics of their clearance or spatial PQC (Fig. 1b).

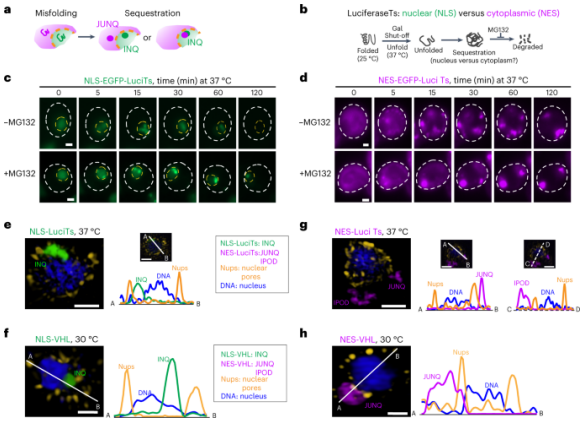

Fig. 1: The INQ and JUNQ are separate nuclear and cytoplasmic PQC compartments. a, Schematic showing nuclear and cytoplasmic misfolded proteins could be sequestered into separate compartments or the cytoplasmic misfolded proteins could be imported into the nucleus and sequestered into the nuclear PQC compartment INQ. b, Experimental schematic. Temperature-sensitive Luciferase is properly folded at 25 °C. Heat shock at 37 °C leads to unfolding and sequestration of the protein. Degradation of the unfolded and sequestered proteins can be blocked by treatment with the proteasome inhibitor MG132. c,d, Live-cell time-lapse fluorescence microscopy of WT cells expressing NLS-LuciTs (c) or NES-LuciTs (d) at 37 °C, treated with DMSO (top) or 100 µM MG132 (bottom). Representative still frames at the times shown. Scale bars, 1 µm. e,f, Representative SIM images of WT cells expressing NLS-LuciTs (e) or NLS-VHL (f) after 2 h at 37 °C (LuciTS) and 30 °C (VHL) and treated with 100 µM MG132. NLS-LuciTs and NLS-VHL are shown in green, nuclear pores in gold and Hoechst counterstain in blue. Scale bars, 1 µm. Line intensity profiles indicate relative locations of subcellular compartments to Nups and DNA. g,h, Representative SIM images of WT cells expressing NES-LuciTs (g) and NES-VHL (h) after 2 h at 37 °C (LuciTS) and 30 °C (VHL) and treated with 100 µM MG132. NES-LuciTs and NES-VHL are shown in purple, nuclear pores in gold and Hoechst counterstain in blue. Scale bars, 1 µm. Line intensity profiles indicate relative locations of subcellular compartments to Nups and DNA.

At 25 °C, NLS- and NES-EGFP-LuciTs were diffusely localized in the nucleus or cytoplasm, respectively (time 0, Fig. 1c,d). The fate of misfolded LuciTs was monitored by time-resolved fluorescence microscopy following a

shift to 37 °C (Fig. 1b). Over the time course at 37 °C, both nuclear (NLS) and cytoplasmic (NES) LuciTs were rapidly concentrated into dynamic puncta in their respective cellular locations (Fig. 1c,d and Supplementary Video 1). NLS-LuciTs coalesced into one intranuclear INQ inclusion (time 30 min, Fig. 1c) while cytoplasmic NES-LuciTs puncta coalesced into two cytoplasmic inclusions, the JUNQ and IPOD (time 30 min, Fig. 1d), as previously shown for Ubc9Ts and VHL[11]. The NLS- and NES-LuciTs inclusions formed both with or without proteasome inhibitor MG132 (Fig. 1c,d), indicating spatial sequestration into PQC compartments is not a consequence of proteasomal inhibition.

Structured illumination microscopy (SIM) with super-resolution defined the location and morphology of nuclear and cytoplasmic PQC inclusions formed by either LuciTs variants at 37 °C and VHL variants at 30 °C and 37 °C. The nuclear envelope was visualized by immunostaining of nuclear pore protein Nsp1 (Nups, yellow) and DNA visualized using Hoechst (blue) (Fig. 1e–h). The INQ localized inside the nucleus in a pocket between the nuclear envelope (delineated by Nups) and the DNA (Fig. 1e and Supplementary Video 2 for NLS-LuciTs at 37 °C, Fig. 1f for NLS-VHL at 30 °C and Extended Data Fig. 1b for NLS-VHL at 37 °C). Line intensity profile analyses confirmed the INQ intranuclear localization (Fig. 1e,f and Extended Data Fig. 1b). Importantly, SIM and line intensity profile analyses unequivocally established the cytoplasmic localization of PQC inclusions formed by NES-LuciTs and NES-VHL: the JUNQ was adjacent to the nuclear envelope, while the IPOD was closer to the cell periphery (Fig. 1g,h, Supplementary Video 2 and Extended Data Fig. 1c). Similar results were obtained with NLS- and NES-VHL at 30 °C and 37 °C, indicating their localization was not temperature dependent (Extended Data Fig. 1b,c). Of note, cytoplasmic misfolded proteins were slightly more toxic than the nuclear variants, albeit less than polyglutamine-expanded Huntingtin exon1 (herein mHTT) associated with Huntington's disease (Extended Data Fig. 1d). We conclude that nuclear and cytoplasmic misfolded proteins respectively form the INQ and JUNQ PQC inclusions in their cognate compartment.

Proteasome inhibition disrupts nucleocytoplasmic transport

Since most commonly used PQC reporters (for example, Ubc9Ts, VHL, Luciferase and so on), are smaller than the 200 kDa nuclear permeability barrier[28,29,30], we considered if their passive diffusion into the nucleus could lead to the formation of intranuclear inclusions[11,17,18]. To test this, we followed Ubc9Ts unfolding at 37 °C using SIM with super-resolution. When the proteasome is active, Ubc9Ts was sequestered solely in two cytoplasmic compartments—the JUNQ outside the nucleus and the IPOD in the cell periphery (Fig. 2a and Supplementary Video 3). Addition of proteasome inhibitor MG132, increased the fraction of cells containing the cytoplasmic Ubc9Ts inclusions, but in addition, some cells (~15%) had a Ubc9Ts inclusion inside the nucleus (Fig. 2b, Extended Data Fig. 2a and Supplementary Video 3). Similar results were observed for unfolded VHL (Extended Data Fig. 2b). Interestingly, line intensity profile analyses showed the nuclear INQ and cytoplasmic JUNQ inclusions formed across each other, separated by the nuclear envelope (marked by Nup, Fig. 2b). Thus, upon proteasome inhibition, cytoplasmic proteins that can passively diffuse into the nucleus can form an additional nuclear INQ in a small fraction of cells.

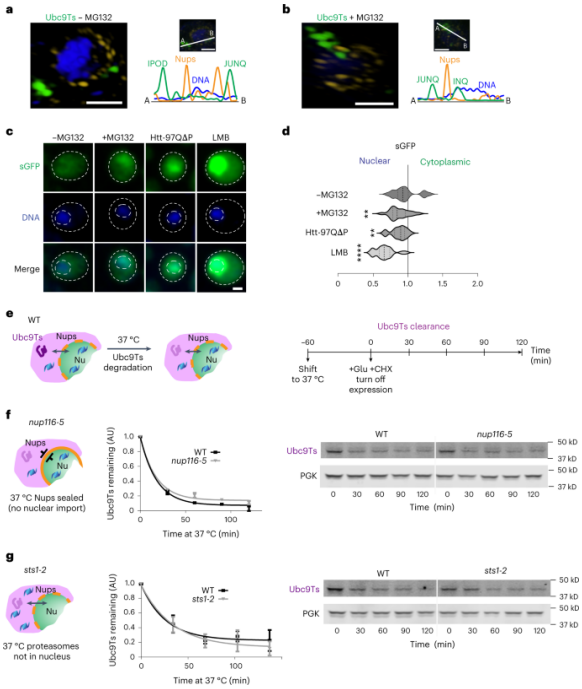

Fig. 2: Nuclear entry of misfolded proteins is not required for clearance. **a**,**b**, Representative SIM images of WT cells expressing Ubc9Ts-EGFP after 2 h at 37 °C treated with DMSO (**a**) or 100 µM MG132 (**b**). Ubc9Ts-EGFP is shown in green, nuclear pores in gold and Hoechst counterstain in blue. Scale bars, 1 µm. Line intensity profiles indicate relative locations of subcellular compartments to Nups and DNA. **c**, Representative confocal fluorescence microscopy images of cells expressing sGFP with DMSO (−MG132), 100 µM MG132 treatment, co-expression of mHTT97QΔP or 200 nM LMB treatment. Scale bar, 1 µm. **d**, Ratio of cytoplasmic:nuclear fluorescence. Kruskal–Wallis test with Dunn's multiple comparisons test was performed using Prism. Adjusted *P* value of no treatment versus MG132 is 0.0014, no treatment versus 97QΔP is 0.0027 and no treatment versus LMB is <0.0001. Twenty cells per condition from five biologically independent experiments were normalized to the no treatment control, analysed and presented as violin plots with median values shown as dashed lines and quartile values shown as dotted lines. **e**, Left: schematic illustrating the clearance of Ubc9Ts in WT yeast. Right: timeline of treatments for clearance measurements with shift to 37 °C 60 min before initiation of the measurements. **f**, Left: schematic illustrating the *nup116-5* yeast have sealed nuclear pores at 37 °C, thus blocking nucleocytoplasmic trafficking. Densitometric quantification (middle) of western blot bands (right) measuring the amount of Ubc9Ts-EGFP remaining in shut-off experiment of WT versus *nup116*-5 cells relative to $t = 0$ (mean ± s.e.m. from three biologically independent experiments) fitted with a one-phase decay non-linear fit regression line. **g**, Left: schematic illustrating the *sts1-2* yeast do not translocate proteasomes to the nucleus at 37 °C. Densitometric quantification (middle) of western blot bands (right) measuring the amount of Ubc9Ts-EGFP remaining in shut-off experiment of WT versus sts1-2 cells relative to $t = 0$ (mean ± s.e.m. from three biologically independent experiments) fitted with a one-phase decay non-linear fit regression line. Source numerical data and unprocessed blots are available in source data.

Since toxic misfolded proteins, such as mHTT, impair nucleocytoplasmic transport[31,32], we hypothesized that proteasome inhibition may alter nucleocytoplasmic trafficking and decrease protein export from the nucleus, retaining some of the diffusible misfolded proteins in the nucleus. We examined the effect of MG132 on nucleocytoplasmic transport using a NLS- and NES-tagged shuttling GFP (sGFP) that migrates between the nucleus and cytoplasm[31,33] (Fig. 2c,d). As expected, toxic mHTT caused nuclear retention of sGFP (Fig. 2c,d), as did nuclear export inhibitor leptomycin B (LMB). Strikingly, proteasome inhibition with MG132 caused sGFP nuclear retention to the same extent as mHTT (Fig. 2c,d), providing a rationale for the increased retention of

misfolded Ubc9Ts in the nucleus upon proteasome inhibition. Future studies should examine the basis for impaired nuclear export upon proteasome inhibition[31,34,35].

We next directly assessed if cytoplasmic misfolded protein clearance requires their import to the nucleus (Fig. 2e). First, we examined Ubc9Ts clearance in *nup116-5* cells. At 37 °C, this mutation in nuclear pore complex (NPC) protein Nup116 results in sealed nuclear pores and blocked transport into and out of the nucleus36 (Fig. 2f, left). No significant difference in the rate and the extent of Ubc9Ts degradation was observed in *nup116-5* cells, suggesting its nuclear import is not required for its clearance (Fig. 2f, middle and right).

We also examined whether nuclear proteasomes participate in cytoplasmic PQC. We used *sts1-2* cells carrying a mutation in Sts1, a protein required for proteasome import into the nucleus[37,38,39,40] (Fig. 2g, left). Consistent with cytoplasmic degradation, loss of nuclear localized proteasomes in *sts1-2* cells had no effect on the clearance of misfolded Ubc9Ts at 37 °C (Fig. 2g, middle and right). We conclude that import of misfolded proteins and proteosomes into the nucleus is dispensable to degrade misfolded Ubc9Ts.

INQ and JUNQ home to opposite sides of the nuclear envelope

To define the spatial relationship between INQ and JUNQ, we co-expressed NLS-LuciTs and NES-LuciTs and monitored inclusion formation after a shift to 37 °C in real time using live-cell time-lapse fluorescence microscopy and particle tracking analysis (Fig. 3a,b, Extended Data Fig. 3a and Supplementary Videos 4 and 5). The NLS- and NES-misfolded proteins were rapidly sequestered into motile condensates with similar kinetics independently in the nucleus and the cytoplasm. Once formed, puncta moved dynamically towards each other, with nuclear and cytoplasmic inclusions converging on a specific location proximal to the nuclear envelope (Fig. 3a). Even after homing to this location, the two inclusions remained distinct and separated; however, they co-migrated around the nuclear periphery as if tethered to each other across the nuclear envelope. Particle tracking analyses measuring the location and distance of NLS- and NES-LuciTs inclusions in 2D space showed the nuclear and cytoplasmic inclusions homed into adjoining locations between 10 min and 20 min after shifting to 37 °C, and then continued moving in a coordinated manner throughout the duration of the imaging experiment (Fig. 3b, Extended Data Fig. 3a and Supplementary Video 5). The distance between these two inclusions decreased rapidly during homing and once they converged, they maintained a largely stable short distance, suggestive of a tether, throughout the remainder of the experiment. Similar results were obtained for NLS- and NES-VHL (Extended Data Fig. 3b). Of note, SIM with super-resolution combined with line intensity profile analysis confirmed the INQ and JUNQ adjoined each other on opposite sides of the nuclear envelope, marked by NPCs (Fig. 3c and Supplementary Video 6). These findings suggest a coordinated convergence of nuclear and cytoplasmic PQC compartments.

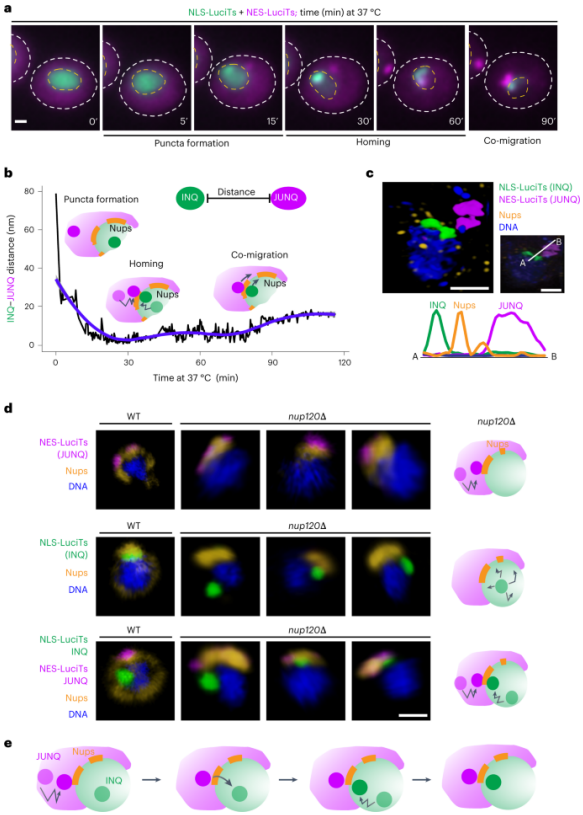

Fig. 3: INQ and JUNQ home to similar location on each side of the nuclear envelope via a cytoplasmic signal linked to nuclear pores. **a**, WT cells co-expressing NLS-EGFP-LuciTs and NES-DsRed-LuciTs were shifted to 37 °C, treated with 100 µM MG132 and monitored by live-cell time-lapse fluorescence. Representative still frames at the times shown. Scale bar, 1 µm. **b**, Graph of the distance between the INQ and JUNQ compartments by particle tracking of inclusions from cell shown in **a** over the time course of the experiment. The slight variations of tethered distance between 60 min and 90 min is possibly due to the relative migration of one of the inclusions around a subcellular structure. **c**, Representative SIM image taken of cells co-expressing NLS-EGFP-LuciTs and NES-DsRed-LuciTs after 2 h at 37 °C and treated with 100 µM MG132. NLS-fusion proteins are shown in green, NES-fusion proteins in purple, nuclear pores in gold and Hoechst counterstain in blue. Scale bar, 1 µm. Line intensity profiles indicate relative locations of subcellular compartments and Nups. **d**, Representative confocal microscopy images taken of WT and three separate *nup120Δ* yeast cells expressing NES-LuciTs (i), NLS-LuciTs (ii) or co-expressing NLS- and NES-LuciTs (iii) after 2 h at 37 °C. NLS-LuciTs is shown in green, NES-LuciTs in purple, nuclear pores in gold and Hoechst counterstain in blue. Scale bar, 1 µm. Schematics on the right summarize the findings of the data. **e**, Schematic summarizing the data that the JUNQ localizes to the nuclear pores. A signal is transmitted through or near the nuclear pores to recruit the INQ to the same location, resulting in the homing of the two compartments. Source numerical data are available in source data.

Nuclear pores play a role in INQ–JUNQ convergence

We next considered the nature of the signal bringing together the INQ and JUNQs. The INQ was near the nucleolus but not in direct contact, suggesting the nucleolus is not driving this homing mechanism (Extended Data Fig. 3c). Neither the spindle pole body[41] nor the LINC complex[42], both of which contain nuclear envelope protein Mps3 (Extended Data Fig. 3d) co-localized with the INQ–JUNQ perinuclear site, suggesting they do not participate in the homing mechanism.

To investigate the role of nuclear pores in INQ/JUNQ homing, we exploited the finding that deletion of nuclear pore protein Nup120 causes NPCs to remain functional but become clustered[43,44]. In *nup120*Δ cells, the JUNQ

always forms next to the clustered nuclear pores (Fig. 3d(i)) while the INQ was found anywhere within the nucleus (Fig. 3d(ii)). Surprisingly, if we co-expressed NLS- and NES-LuciTs in *nup120*Δ cells, the INQ now homed to the clustered nuclear pores opposite the JUNQ (Fig. 3d(iii)), indicating JUNQ formation at the cytoplasmic side of NPCs communicates a signal for INQ recruitment to this location (Fig. 3e). The disordered phenylalanine–glycine (FG) repeats in the central nuclear pore channel[45] do not play a role in INQ and JUNQ homing, which was unaffected in *nupΔFG* cells carrying deletions of ~70% of the FG content from NPCs[46] (Extended Data Fig. 3e).

Cryo-SXT reveals the architecture of PQC inclusions in intact cells

To examine the in vivo context of PQC compartments we used cryogenic soft X-ray tomography (cryo-SXT), which can visualize and quantify the ultrastructure of intact, unstained, cryo-preserved cells (Fig. 4a and Extended Data Fig. 4a,b)[47,48,49]. The characteristic X-ray linear absorption coefficients (LACs) vary with the type and density of biomolecules present in different compartments[50,51,52] and can be used to produce projection images of cellular ultrastructure to a few nanometres of spatial resolution (Fig. 4b, right).

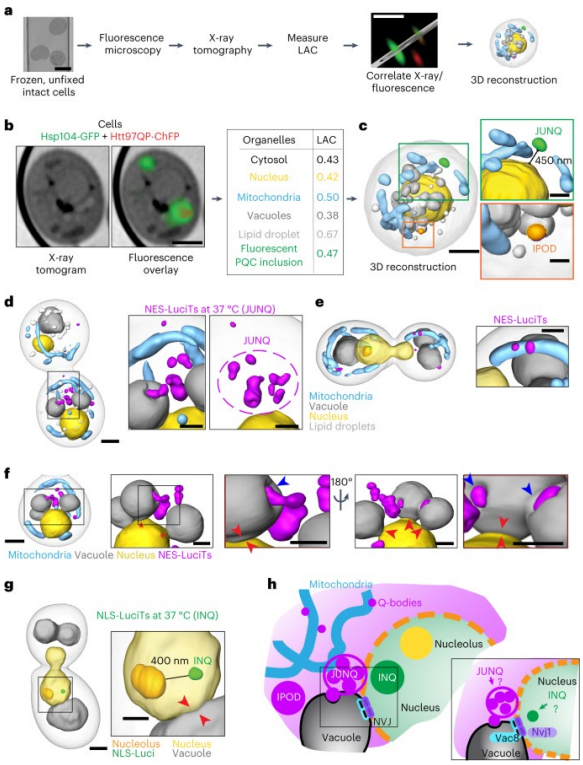

Fig. 4: INQ resides near the nucleolus, JUNQ is surrounded by mitochondria and both compartments home into the NVJ. **a**, Unfixed, intact yeast cells are frozen in a capillary tube and imaged by fluorescence microscopy and then X-ray tomography. Scale bar, 5 µm. The LACs are measured from the tomography data and used to identify the subcellular compartments and organelles. The fluorescence images are correlated to the X-ray tomography data, and 3D reconstructions of the subcellular components are generated. **b**, WT cells co-expressing Hsp104-GFP from the endogenous locus and HTT97QP-ChFP after 30 min at 37 °C. Left: X-ray tomograms without and with fluorescence overlay to indicate sites of Hsp104-GFP positive inclusions and HTT97QP-ChFP inclusion. Right: table of LAC values from the X-ray tomograms used to annotate the images and generate a 3D reconstruction shown in **c**. **c**, 3D reconstruction of fluorescence-correlated X-ray tomograms showing the JUNQ residing 450 nm outside the barrier of the nucleus (inset, top) and the IPOD marked by mHTT (inset, bottom). **d**, 3D reconstruction of X-ray tomograms from cell expressing NES-LuciTs after 90 min heat shock at 37 °C and treated with 100 µM MG132. The Q-bodies coalesce into the JUNQ compartment (inset, right). The Q-bodies also interact with vacuoles and the JUNQ compartment is surrounded by a mitochondrial cage (inset, left). **e**, Q-bodies interact with mitochondria in a separate cell expressing NES-LuciTs. **f**, Same 3D reconstruction of X-ray

tomograms from cell shown in **d**. Insets are from the same cell rotated 180°. Blue arrows indicate sites where Q-bodies are directly interacting with the vacuoles. Red arrows indicate sites of NVJs. **g**, 3D reconstruction of X-ray tomograms from cell expressing NLS-LuciTs after 90 min heat shock at 37 °C and treated with 100 µM MG132. The INQ resides 400 nm from the nucleolus (inset). **h**, Schematic illustrating the findings of the X-ray tomography. The inset highlights two of the component proteins of the NVJ, Nvj1 and Vac8. Scale bars on X-ray 3D reconstructions are 1 µm; insets are 0.5 µm. JUNQ is shown in green, IPOD in orange, Q-bodies in purple, nucleus in yellow, nucleolus in gold, mitochondria in cyan, vacuoles in grey and lipid droplets in white.

To derive the information content needed to study misfolded protein inclusions we initially used cryo-SXT in correlation with cryo-fluorescence microscopy (Fig. 4b, left). Since chaperone Hsp104 localizes to both the JUNQ and IPOD, while mHTT only localizes to the IPOD[11,20], cryo-fluorescence identified the PQC compartments. Chromosomally tagged Hsp104-GFP[53] signal only marks the JUNQ and co-localized Hsp104-GFP and mHTT-ChFP marks the IPOD. Cells were flash frozen in capillary tubes and directly imaged using cryo-SXT correlated with cryo-fluorescence microscopy (Fig. 4b, left). LAC values were used to identify specific compartments and organelles in X-ray tomograms of intact frozen yeast cells (Fig. 4b, right), yielding a 3D reconstruction of the PQC inclusions in the context of cellular architecture (Fig. 4c and Supplementary Video 7). This analysis revealed that protein inclusions have a characteristic LAC that can be used to examine their location and size without the need of fluorescence microscopy. Of note, correlated fluorescence-cryo-SXT analyses confirmed that both the JUNQ and the IPOD are cytoplasmic, as previously described (Fig. 4c and Supplementary Videos 7 and 11).

Next, we detected inclusions formed by NLS- and NES-LuciTs at 37 °C through their characteristic LAC values (Fig. 4c). NES-LuciTs formed small, cytoplasmic, punctate Q-bodies that congregated at a cytoplasmic, juxtanuclear location to form the JUNQ (Fig. 4d and Supplementary Video 8). Cryo-SXT analysis indicates the JUNQ is not the homogeneous large compartment suggested by diffraction-limited fluorescence imaging, but rather consists of multiple dense 'cores' that resemble Q-bodies. This conclusion is consistent with the irregular JUNQ morphology in SIM and cryogenic electron microscopy imaging (Figs. 1 and 5)[54]. It thus appears the JUNQ is in fact a collection of Q-bodies that congregate at a perinuclear location proximal to the nuclear envelope (Fig. 4d (inset right) and Supplementary Video 8).

Cryo-SXT analysis revealed Q-bodies associated with the surface of mitochondria (Fig. 4e), and the JUNQ and IPOD were surrounded by a mitochondrial cage (Fig. 4d). Confocal fluorescence microscopy of cells expressing mito-GFP supported the mitochondrial association with Q-bodies (Extended Data Fig. 4d). However, PQC compartments still formed in cells with disruptions in mitochondrial fission or fusion (Extended Data Fig. 4e), indicating mitochondrial structure does not direct PQC compartment formation. Since previous studies placed Q-bodies on the ER membrane[17,20], which cannot be visualized by cryo-SXT, it is possible that Q-bodies are proximal to ER–mitochondrial contact sites. Alternatively, proximity to mitochondria may serve to place energy-intensive PQC compartments in areas of the cell enriched in ATP production[55].

Cryo-SXT confirmed the intranuclear INQ is distinct from but resides near the nucleolus (Fig. 4g). The proximity of the nucleolus to the INQ was supported by confocal fluorescence microscopy with nucleolar protein Nsr1 (Extended Data Figs. 3c and 4c)[18,31]. Given the nucleolus' role in nuclear folding and assembly[21,56,57,58], this suggests a possible nucleolus link to the INQ's function in nuclear PQC[56,59].

Cryo-SXT imaging revealed an unexpected link of both INQ and JUNQ with the vacuole. The entire JUNQ site was surrounded by nuclear–vacuolar inter-organelle contact sites, and the INQ was proximal to the vacuolar side of the nucleus (Fig. 4f (red arrows), Fig. 4g and Supplementary Video 8). Remarkably, Q-bodies within the JUNQ area were nestled within invaginations in the vacuolar membrane, suggestive of direct vacuolar engulfment (Fig. 4f (blue arrows) and Supplementary Video 8). This raises the idea that the vacuole promotes JUNQ clearance and INQ and JUNQ are steered to the vicinity of nuclear–vacuolar contact sites, which are formed by a

tethering NVJ complex between nuclear Nvj1 and vacuolar Vac8 (Fig. 4h)[60]. Consistent with the idea that the INQ and JUNQ converge to the vicinity of NVJs, all nuclear pores in *nup120Δ* cells cluster at the vacuole-contacting side of the nucleus[44].

NVJs allow clearance of JUNQ and INQ

While the function of NVJs remains poorly understood, they have been implicated in lipid droplet biogenesis, amino acid metabolism and piecemeal microautophagy of the nucleus, whereby portions of the nucleus invaginate into the vacuole[61,62,63,64,65,66]. We confirmed the JUNQ co-localizes with the NVJ by expressing NES-LuciTs or Ubc9Ts in cells carrying a chromosomally tagged Nvj1-GFP[53]. Live-cell time-lapse microscopy revealed transient and dynamic interactions between JUNQ and Nvj1 (Fig. 5a and Extended Data Fig. 5a; for example, observe 9 min to 11 min in Supplementary Video 9).

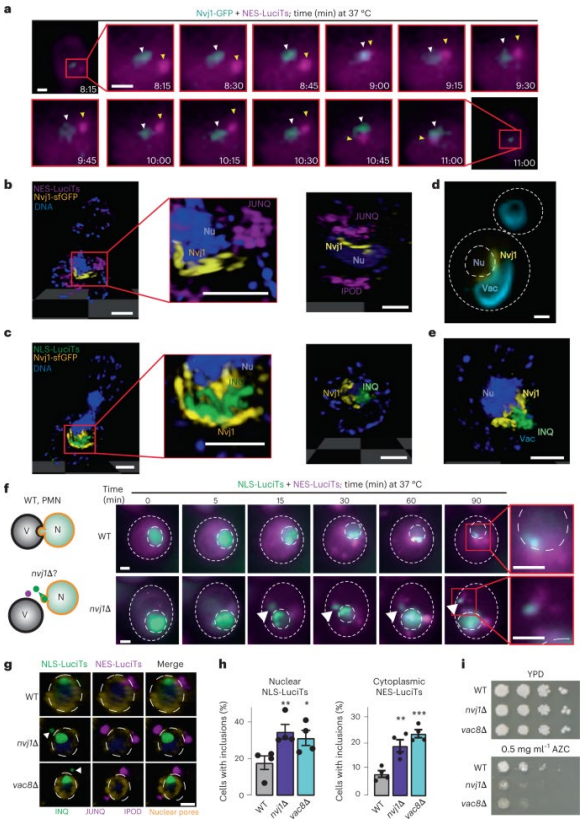

Fig. 5: JUNQ and INQ converge at the NVJ to facilitate clearance. **a**, Endogenously tagged Nvj1-GFP yeast expressing NES-DsRed-LuciTs were shifted to 37 °C and monitored by live-cell time-lapse fluorescence microscopy for the times shown. White arrowheads indicate locations of Nvj1 punctum, while yellow arrowheads indicate NES-LuciTs punctum. **b**,**c**, Representative SIM images of WT yeast co-expressing NES-DsRed-LuciTs (**b**) or NLS-DsRed-LuciTs (**c**) and Nvj1-sfGFP after 2 h incubation at 37 °C with 100 µM MG132. Middle panel of both **b** and **c** is an inset to better visualize the relative location of the JUNQ and INQ to the Nvj1. Right panel of both **b** and **c** shows additional cells to illustrate other phenotypes seen in the experiment. NES-DsRed-LuciTs (purple), NLS-DsRed-LuciTs (green), Nvj1-sfGFP (yellow) and DNA (blue). **d**, Representative confocal image of WT yeast expressing Nvj1-sfGFP (yellow) stained with FM4-64 vacuolar dye (cyan). **e**, Representative SIM image of WT yeast cell co-expressing NLS-DsRed-LuciTs (green) with Nvj1-sfGFP (yellow) after 2 h incubation at 37 °C with 100 µM MG132. The NLS-LuciTs can be seen extruding through the NVJ towards the vacuole. **f**, WT (top) and *nvj1Δ* (bottom) cells co-expressing NLS-LuciTs and NES-LuciTs were shifted to 37 °C, treated with 100 µM MG132 and monitored by live-cell time-lapse fluorescence microscopy for the times shown. White arrowheads indicate inclusions of NLS-LuciTs pulled into the cytoplasm. **g**, Representative confocal images of WT, *nvj1Δ* and *vac8Δ* yeast co-expressing NLS-EGFP-LuciTs and NES-DsRed-LuciTs after 2 h at

37 °C and treated with 100 µM MG132. NLS-EGFP-LuciTs (green), NES-DsRed-LuciTs (purple), nuclear pores (gold) and Hoechst counterstain (blue). White arrows indicate cytoplasmic localization of NLS-LuciTs. **h**, Quantitation of the percentage of cells containing inclusions in WT, *nvj1Δ* and *vac8Δ* yeast co-expressing NLS-EGFP-LuciTs (left) and NES-DsRed-LuciTs (right) after 2 h incubation at 37 °C with 100 µM MG132. Data are shown as mean ± s.e.m. **i**, Drop tests showing serial dilutions of WT, *nvj1Δ* and *vac8Δ* yeast at 30 °C and 37 °C with no treatment and 0.5 mg ml^{-1} AZC treatment after 72 h growth at indicated temperature. All scale bars are 1 µm. Source numerical data are available in source data.

SIM with super-resolution revealed the architecture of perinuclear spatial PQC relative to the NVJ (Fig. 5b–e and Supplementary Videos 10 and 11). The NVJ, visualized via Nvj1-sfGFP imaging, forms a basket-shaped structure contouring the nuclear envelope and connected to the vacuole (Fig. 5d). The JUNQ, visualized by NES-LuciTs, was proximal to the cytoplasmic side of the NVJ as observed by Cryo-SXT (Fig. 5b). Of note, the Q-body 'assembly' substructure of the JUNQ was evident in these SIM images. The nuclear INQ, visualized by NLS-LuciTs, was nested between the concave nuclear side of the NVJ and the nuclear DNA (Fig. 5c). Strikingly, in some cells the INQ was observed extruding through the NVJ (Fig. 5e and Supplementary Video 12).

We next examined if the NVJ participates in INQ and JUNQ homing and clearance using live-cell time course analyses in *nvj1Δ* or *vac8Δ* cells. Deleting the NJVs did not disrupt INQ and JUNQ convergence (Fig. 5g). However, while NLS-LuciTs formed an initial nuclear inclusion in *nvj1Δ* cells, we observed the INQ egressed from the nucleus into the cytoplasm in some cells (Fig. 5f). Strikingly, the egressed NLS-LuciTs puncta ended up co-localizing with NES-LuciTs (Fig. 5f (inset) and Supplementary Video 13 (white arrowheads)). Confocal microscopy in *nvj1Δ* or *vac8Δ* cells confirmed that NVJ disruption led to extrusion of nuclear NLS-LuciTs into the cytosol and co-localization with NES-LuciTs puncta (Fig. 5g, white arrowheads).

On the basis of our sXRT observation that Q-bodies are invaginated into vacuoles and the role of NVJ in piecemeal microautophagy of the nucleus[61] (Fig. 4), we hypothesized that the NVJ may enable vacuolar targeting of the nuclear and the cytoplasmic inclusions. The use of EGFP-fused PQC substrates allowed us to address this hypothesis via fluorescence quenching, similar to the approach monitoring GFP targeting to mammalian lysosomes. While in mammalian cells the lysosomal pH (4.5–5.5) (refs. [67,68]) suffices to quench GFP fluorescence (pK_a 4.5 (refs. [69,70,71])), the higher yeast vacuolar pH (4.9–6.2; 4.9 ± 0.2 in the BY4741 strain[72]) suffices to quench the brighter EGFP[73] fluorescence (pK_a 6.0 (refs. [69,70,71])). Following a chase at 37 °C we observed that NVJ deletion led to dramatic increases in the fraction of cells containing JUNQ or INQ compared with wild-type (WT) cells (Fig. 5h (left and right) and Extended Data Fig. 5c,d); similarly, immunoblot analyses showed NVJ deletion increased levels of misfolded proteins (Extended Data Fig. 5e). Of note, partial proteasome inhibition by MG132 during the 37 °C chase led to a synergistic enhancement in the number of cells with NES- or NLS-LuciTs inclusions (Extended Data Fig. 5c,d), suggesting the NVJ and the proteasome represent distinct clearance pathways. Supporting a role in misfolded protein clearance, NVJ deletions sensitize cells to proteotoxic stress caused by treatment with proline analogue AZC, which induces widespread misfolding of newly translated proteins (Fig. 5i). Taken together, our findings define nuclear–vacuolar contacts as cellular hubs for nuclear and cytoplasmic spatial PQC.

Perinuclear ESCRT facilitates INQ–JUNQ homing and clearance at NVJs

We next considered how INQ–JUNQ homing at nuclear–vacuolar contacts is achieved. We hypothesized a possible role of perinuclear ESCRT-II/III protein Chm7, previously implicated in nuclear envelope sealing and NPC quality control[74,75,76] (Fig. 6a, left). Chm7 is normally diffuse throughout the cytoplasm (Extended Data Fig. 6a) but localizes to a unique site in the nuclear envelope upon activation. The active Chm7 conformation can be induced by deleting auto-inhibitory helices in the ESCRT-III domain (herein $Chm7_{OPEN}$)[76,77]. Notably, the

Chm7$_{OPEN}$ site in the nuclear envelope marks the homing location for both INQ and JUNQ (Fig. 6a, right). Furthermore, Chm7 is required for homing. In *chm7Δ* cells, both INQ and JUNQ still formed and migrated to the perinuclear region but in some cells no longer converged to the same location (Fig. 6b). We conclude perinuclear ESCRT-II/III protein Chm7 mediates the convergence of INQ and JUNQ on the nuclear envelope.

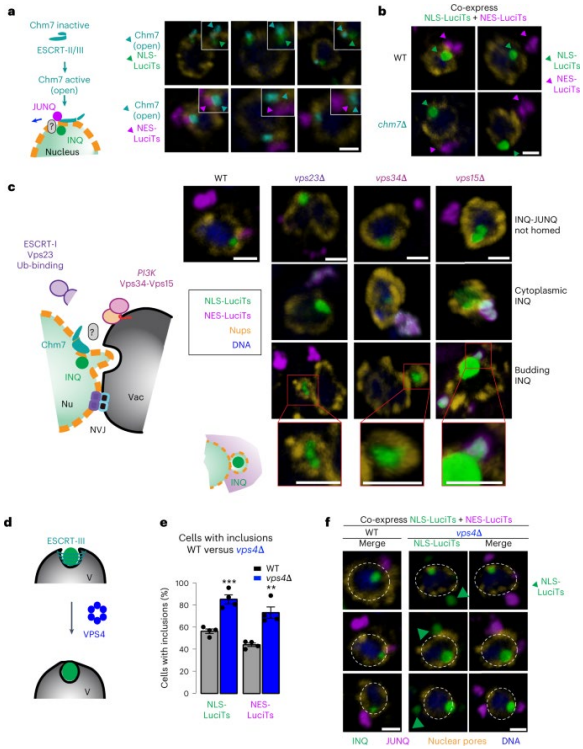

Fig. 6: ESCRT-mediated extrusion from the nucleus and clearance. **a**, Left: the ESCRT-II/III protein Chm7 has been shown to play a role in clearance of defective nuclear pores and nuclear membrane quality control; therefore, it may be involved in the homing of INQ and JUNQ to the NVJ. Right: representative confocal images of WT yeast co-expressing Chm7$_{OPEN}$-EGFP and either NLS-DsRed-LuciTs (top) or NES-DsRed-LuciTs (bottom) after 2 h at 37 °C and treated with 100 µM MG132. Arrows indicate locations of puncta for each protein. Scale bar, 1 µm. **b**, Representative confocal images of WT and *chm7Δ* yeast co-expressing NLS-EGFP-LuciTs and NES-DsRed-LuciTs after 120 min at 37 °C and treated with 100 µM MG132. Arrows indicate locations of puncta for each protein. **c**, ESCRT protein Vps23, and PI3K complex Vps34–Vps15 may be involved in clearance of INQ and JUNQ. Representative confocal images of WT and *vps23Δ*, *vps34Δ* and *vps15Δ* yeast co-expressing NLS-EGFP-LuciTs and NES-DsRed-LuciTs after 2 h at 37 °C and treated with 100 µM MG132. Insets show the budding INQ encapsulated by nuclear pores. **d**, ESCRT-III proteins and the ATPase Vps4 are known to remodel membranes and could be involved in vacuolar import of PQC compartments. **e**, Quantitation of the percentage of cells containing inclusions of NLS- or NES-LuciTs in WT and *vps4*Δ yeast co-expressing NLS-EGFP-LuciTs and NES-DsRed-LuciTs after 2 h incubation at 37 °C with 100 µM MG132. Data are shown as mean ± s.e.m. **f**, Representative confocal images of WT and *vps4*Δ yeast co-expressing NLS-EGFP-LuciTs and NES-DsRed-LuciTs after 2 h at 37 °C and treated with 100 µM MG132. Green arrows indicate cytoplasmic localization of NLS-LuciTs. All scale bars are 1 µm. Chm7$_{OPEN}$ is shown in teal, NLS-DsRed-LuciTs in green, NES-DsRed-LuciTs in purple, nuclear pores in gold and Hoechst counterstain in blue. Source numerical data are available in source data.

To examine if additional ESCRT and endosomal proteins participate in spatial PQC, we tested deletions in Vps23, Vps34 and Vps15. Vps23 is part of the ESCRT-I complex recognizing ubiquitinated proteins and mediating their vacuolar transport[78,79,80]. Vps34–Vps15 form a membrane-bound phosphatidylinositol 3-kinase (PI3K) complex essential for protein sorting to the vacuole[81,82,83,84]. Of note, Vps34–Vps15 are reported to localize to NVJs[81,82,83,84]. We co-expressed NLS- and NES-LuciTs in either WT, *vps23Δ*, *vps34Δ* or *vps15Δ* cells and followed

their fate after inducing unfolding at 37 °C. INQ and JUNQ formed in both WT and mutant cells. However, all three mutants disrupted the spatial relationship between INQ and JUNQ, displaying similar aberrant localization phenotypes. These included cells in which the INQ and JUNQ were no longer homed (Fig. 6c and Extended Data Fig. 6b) and cells displaying cytoplasmic egress of the INQ (Fig. 6c and Extended Data Fig. 6b). Strikingly, in some *vps23Δ* and *vps34Δ* cells we observed a possible intermediate for nuclear egress of the INQ, whereby the NLS-LuciTs inclusion was fully enveloped by the nuclear membrane in what appears to be a budding event (Fig. 6c and Extended Data Fig. 6b).

Vacuolar engulfment often requires AAA-ATPase Vps4, which functions by disassembling ESCRT-III complexes[85,86] (Fig. 6d). We thus examined whether Vps4 is required for INQ and JUNQ clearance. Indeed, *vps4Δ* cells contained more NLS- and NES-LuciTs inclusions than WT controls (Fig. 6e). Strikingly, NLS-LuciTs also egressed into the cytoplasm in some *vps4Δ* cells (Fig. 6f), supporting the notion Vps4 mediates INQ budding into the vacuole. We conclude a perinuclear ESCRT pathway facilitates INQ and JUNQ homing to the NVJ as well as INQ extrusion, probably to mediate Vps4-dependent vacuolar delivery and clearance. When this process is perturbed, the INQ can instead bud into the cytoplasm.

Vacuolar clearance of proteins in INQ and JUNQ

To directly assess if nuclear and cytoplasmic inclusions are targeted to the vacuole, we N-terminally tagged NLS- and NES-LuciTs with the pH-sensitive protein sensor Keima (2xKeima-LuciTS; Fig. 7a,b, schematic). Keima has a pH-insensitive maximum emission at 620 nm (ref. [87]), but its pH-sensitive excitation spectrum has a maximum of 440 nm at neutral pH and a maximum of 558 nm in acidic environments[87,88]. At the pH of the yeast vacuole (pH ~5 in our strain background) the excitation at 440 nm is strongly decreased and the red-shifted 560 nm excitation peak is strongly enhanced, providing a stringent readout of vacuolar targeting for our PQC reporters.

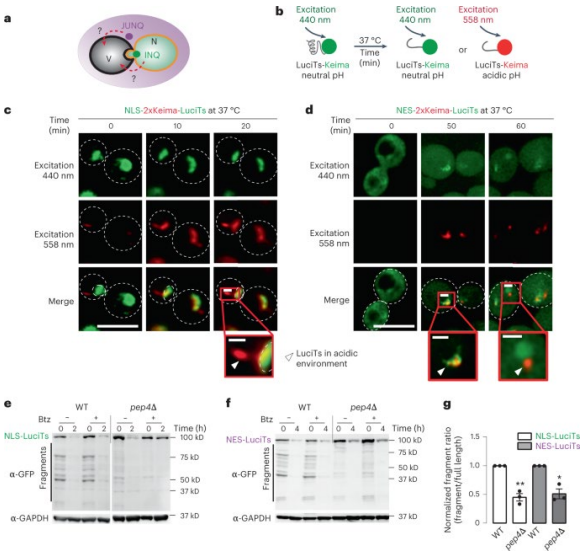

Fig. 7: Vacuolar clearance of the INQ and JUNQ. **a**, Possible routes of entry into the vacuole for the INQ and JUNQ. **b**, Schematic of the LuciTs-Keima experiments. **c**, WT cells expressing NLS-2xKeima-LuciTs after 2 h incubation at 37 °C with 100 µM MG132. Over time, fluorescence is seen with excitation in the 558 nm channel indicating the NLS-LuciTs has encountered an acidic environment. Inset shows the transition from green to red and a structure leaving the inclusion that is fully red. Scale bars on large images are 5 µm. Scale bars on magnifications are 1 µm. Images are representative of two biologically independent experiments. **d**, Representative images of WT cells expressing NES-2xKeima-LuciTs after 2 h incubation at 37 °C with 100 µM MG132. Over time, fluorescence is seen with excitation in the 589 nm channel indicating the NLS-LuciTs has encountered an acidic environment. Insets show the transition from green to red and a structure leaving the inclusion that is fully red. Scale bars on large images are 5 µm. Scale bars on magnifications are 1 µm. Images are

representative of two biologically independent experiments. **e**,**f**, Representative western blots of NLS-EGFP-LuciTs (**e**) and NES-EGFP-LuciTs (**f**) in WT and *pep4*Δ yeast. *pep4*Δ yeast were also treated with 1 mM PMSF to completely inhibit vacuolar proteases. A decrease in fragments can be seen in both the NLS (**e**) and NES (**f**) blots. **g**, Densitometric quantification of western blot bands measuring the amount of full-length LuciTs-EGFP and the fragments seen at T_0. The ratio of fragment intensity to full-length protein is shown in the graph (mean ± s.e.m. from three biologically independent experiments). One-way analysis of variance was performed using Prism software followed by Dunnett's multiple comparisons test. Adjusted *P* value for WT versus *pep4*Δ NLS-LuciTs is 0.0018, and WT versus *pep4Δ* NES-LuciTs is 0.0220. Source numerical data and unprocessed blots are available in source data.

In the folded state, both NLS and NES variants were diffusely located in the nucleus and the cytoplasm, respectively, and exhibited only the neutral pH 440 nm excitation wavelength, with no 560 nm excitation. Upon misfolding at 37 °C, NLS- and NES-LuciTs-2xKeima respectively formed the INQ and JUNQ, with both inclusions in neutral pH environments. However, upon continued incubation at 37 °C we observed a time-dependent appearance of regions with an acidic excitation spectrum for both inclusions (Fig. 7c,d and Extended Data Fig. 7a,b). The acidification kinetics of the JUNQ was slower than for the INQ, consistent with its slower clearance kinetics (Extended Data Fig. 1a). For the INQ, the red shift appears to initiate at the nuclear envelope boundary, with an elongated, red-shifted structure extending from the inclusion into the vacuole (Fig. 7c). The slower degradation kinetics of the JUNQ coupled with the quick photobleaching of Keima precluded continuous live imaging, but an imaging time course of different regions on the same slide showed multiple red-shifted foci arising proximal to the Q-bodies composing the JUNQ (Fig. 7d and Extended Data Fig. 7a,b). As these experiments were carried out under conditions of ongoing proteasomal degradation, we conclude vacuolar targeting occurs in parallel to UPS-mediated clearance of misfolded proteins. Biochemical analyses supported this conclusion (Fig. 7e,f). EGFP immunoblot analyses probing for clearance of our reporters after 2 and 4 h at 37 °C showed a time-dependent reduction of full-length nuclear and cytoplasmic LuciTs. The contribution of proteasomal clearance was assessed by addition of 50 µM Bz (refs. [25,89]) at *T* = 0, while the contribution of vacuolar clearance was assessed in *pep4Δ* cells supplemented with 1 mM phenylmethylsulfonyl fluoride (PMSF) to inhibit vacuolar proteases[90]. While the proteasome tends to degrade the entire GFP fusion, vacuolar clearance leads to accumulation of truncations containing undigested GFP moieties[64,65,90,91,92,93,94]. Both NLS- and NES-LuciTs were partially stabilized by proteasomal inhibition or by inhibition of vacuolar proteases[71,95](Fig. 7c–e and Extended Data Fig. 7c,e). Interestingly, EGFP-positive degradation products typical of vacuolar targeting[64,65,90,91,92,93,94] were observed in WT and +Bz cells but not when vacuolar proteases were inhibited (Fig. 7g). Supporting vacuolar degradation of both nuclear and cytoplasmic PQC substrates, quantification of the intensity of degradation fragments relative to initial full-length protein confirmed the reduction in clearance in *pep4Δ* cells (Fig. 7g). A longer exposure reveals fewer bands and a completely different banding pattern between WT and vacuolar protease inhibited cells (Extended Data Fig. 7c).

To independently corroborate the role of an NVJ- and Vps4-dependent pathway transfers nuclear PQC substrates to the vacuole, we carried out live-cell time-resolved imaging (Fig. 8a). The INQ was visualized via NLS-LuciTs-EGFP and the vacuole using the styryl dye FM4-64 (ref. [96]) (Fig. 8a and Supplementary Video 14). In WT cells, the INQ is proximal to the vacuole at the start of the time course and appears to be pulled into the vacuole as a function of time[71,95,97,98] (Supplementary Video 14 and Extended Data Fig. 7f). Since EGFP fluorescence is quenched by the acidic vacuolar environment, the disappearance of the NLS-LuciTS fluorescence (illustrated in Fig. 8a for a single cell between 45 min and 47 min) is consistent with dynamic clearance of the INQ through the vacuole. Upon disruption of nuclear–vacuolar contacts in *nvj1Δ*, the INQ was unable to interact with and enter the vacuole and instead moved dynamically without loss in fluorescence (Fig. 8a (second row) and Supplementary Video 15). Strikingly, in most *vps4Δ* cells, the INQ does not get cleared and remains proximal

to the vacuole (Fig. 8a (third row) and Supplementary Video 16). These results support the existence of an NVJ and Vps4-dependent pathway for INQ vacuolar engulfment (Fig. 8a and Supplementary Video 16).

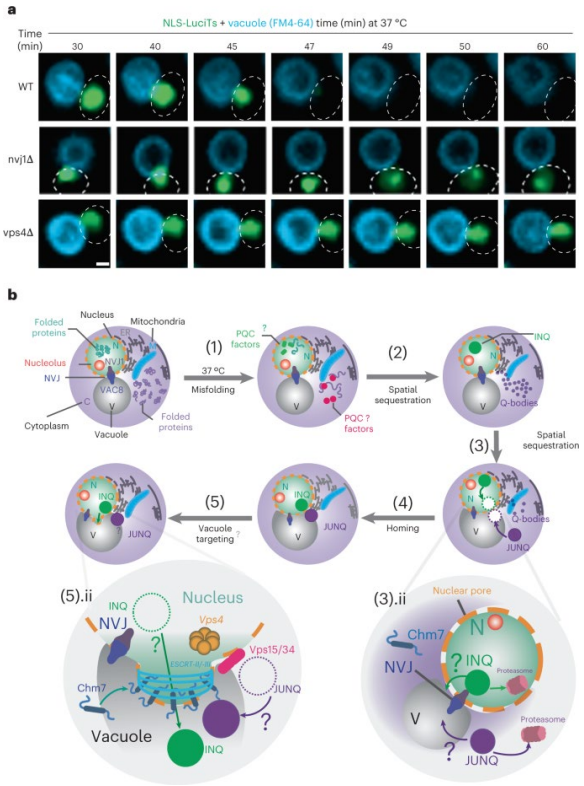

Fig. 8: Nuclear and cytoplasmic spatial PQC. **a**, WT, *nvj1Δ*, and *vps4Δ* yeast expressing NLS-GFP-LuciTs were treated with 8 µM of FM4-64 and incubated for 2 h at 37 °C with 100 µM MG132. Cells were imaged every 5 min for 90 min. Scale bar is 1 µm. **b**, Model for vacuolar targeting and clearance of nuclear and cytoplasmic protein inclusions in yeast. (1) Upon heat shock, cytoplasmic and nuclear LuciTs locally misfold, and recruit chaperones and other PQC factors that facilitate the subcellular spatial sequestration on distinct protein quality control inclusions: (2) The Intranuclear Quality Control compartment (INQ) in the nucleus and Q-bodies in the cytoplasm. (3) Q-bodies then coalesce to form the JUNQ, and misfolded proteins located in the INQ and the JUNQ can be degraded by the UPS system in the nucleus and the cytoplasm, respectively (3, ii). (4) Alternatively, under conditions of limited proteasomal activity, INQ and JUNQ can converge on the periphery of the nuclear envelope, a mechanism mediated by the nuclear pores (homing). (5) The homing mechanism could represent a coordinated way to target both inclusions for clearance at the vacuole. (5, ii) Vacuolar-mediated clearance of both INQ and JUNQ. ESCRT-family proteins are involved in organizing the INQ and JUNQ for vacuolar degradation.

Discussion

Here we uncover a surprising degree of coordination between nuclear and cytoplasmic spatial PQC. Cytoplasmic misfolded proteins are sequestered into a perinuclear JUNQ compartment, while nuclear misfolded proteins are sequestered into a nuclear perinucleolar INQ compartment (Fig. 8). Nuclear import is dispensable for cytoplasmic PQC, consistent with previous studies that nuclear and cytoplasmic proteins are cleared in the compartment where they misfold via compartment-specific ubiquitin ligases and ubiquitin linkage requirements[25,99] (Fig. 8). Cryo-SXT and super-resolution imaging indicate the JUNQ is cytoplasmic and consists of an assembly of membrane-less PQC inclusions called Q-bodies[54,100]. Notably, the Q-bodies and JUNQ exhibit a distinct LAC in cryo-SXT data (Fig. 4b–f), suggesting they may be liquid-like phase-separated entities[54]. Q-bodies were previously shown to form in a chaperone-dependent manner early during misfolding in association with

the ER; here we find they are also close to mitochondria[2,9]. It will be of interest to assess how Q-bodies congregate to form the JUNQ, but perhaps via a pathway akin to the Syntaxin-5-dependent pathway described to traffic Hsp104-associated aggregates[20].

While forming independently, the nuclear INQ and cytoplasmic JUNQ converge to face each other across the nuclear envelope at a site proximal to the NVJs (Fig. 8). The homing process seems to be coordinated by nuclear pores and a perinuclear ESCRT pathway (Fig. 8). ESCRT-II/III protein Chm7 is required for homing of JUNQ and INQ. The AAA-ATPase Vps4 is required for vacuolar degradation, which in the case of the INQ appears to require nuclear egress into the vacuole (Fig. 8, inset). Deletions in the NVJ or perinuclear ESCRT pathway components lead to egress of NLS-LuciTs puncta into the cytoplasm. The observation in these mutants of egressed nuclear puncta still surrounded by nuclear pores suggests a model of INQ budding from the nucleus into the vacuole. Previous studies showed the physical tether provided by NVJs mediates engulfment of regions of the nuclear membrane into the vacuole. The role of NVJs mediating egress of the INQ into the vacuole probably ensures that the nuclear compartment can clear misfolded proteins via vacuolar targeting even when the proteasome is overloaded or otherwise impaired.

Spatial sorting of misfolded proteins into inclusions probably serves to sequester toxic species and enhance cellular fitness[17,20,101]. The convergence of INQ and JUNQ to nuclear–vacuolar contacts may additionally serve to connect spatial PQC to the vacuole, providing an alternate route to proteasomal degradation. Because vacuolar protein clearance of both INQ and JUNQ is observed without proteasome inhibition, it appears proteasomal and vacuolar clearance do not necessarily function hierarchically during spatial PQC. This raises interesting questions for future studies, including whether these pathways act on the same pool of PQC substrates, or select their substrates based on distinct chaperone and/or ubiquitin signals[102]. Future studies should also determine whether additional forms of autophagy participate in clearance of these PQC compartments.

We find perinuclear ESCRT-II/III protein Chm7 (CHMP7 in mammals), plays a key role recruiting the INQ and JUNQ to a unique location on the nuclear envelope. Since Chm7 association with a unique site in the nuclear envelope requires activation of an autoinhibited conformation, it will be of interest to identify the mode of Chm7 activation by PQC inclusions. CHMP7 was previously shown to function in remodelling nuclear envelopes[74], clearance of misassembled nuclear pores[75], egress of herpes virus from the nucleus to the cytosol[103], and nuclear envelope sealing and nuclear pore quality control[77]. Our data thus provide an intriguing link between PQC and nuclear envelope quality control.

Our findings place spatial PQC in the larger context of cellular organization and inter-organellar communication[104]. This idea is particularly intriguing given the link between nuclear pore and nuclear envelope dysfunction and ageing. Of note, lamin progeria mutants and neurodegenerative diseases such as Huntington's disease, amyotrophic lateral sclerosis and frontal temporal dementia are all characterized by nuclear pore dysfunction and altered nucleocytoplasmic trafficking[31,34,35,105,106,107,108]. Our findings raise the possibility that compromising nucleocytoplasmic trafficking leads to impaired misfolded protein clearance contributing to further cellular dysfunction. A better understanding of these pathways may provide fundamental insights into the critical biological process of PQC and point to avenues to ameliorate a large range of human disorders.

Methods

Time-resolved live-cell imaging

BY4741 cells were grown overnight in raffinose medium followed by 4–6 h at 28 °C in galactose medium to induce the expression. Cells were then immobilized on concanavalin-A-coated coverslips. Samples were washed in glucose medium and kept in the same medium by sealing the coverslips to slides with vacuum grease. When indicated, cells were treated 10 min before sealing with 100 μM of MG132 (Sigma) before sealing. Images were

taken every 15 s for 60 min at 37 °C (or room temperature (25 °C)) using a Zeiss Axio Observer.Z1 inverted microscope equipped with X-cite 120 LED light source (Lumen Dynamics), HE GFP/Cy3/DAPI shift free filter sets (Zeiss), a Plan-Apochromat 100×/1.4 oil DIC M27 objective (Zeiss) and a digital Axiocam MRm camera (Zeiss) controlled with the Zen blue software.

CHX chase of pre-formed inclusions

Cells were grown overnight in raffinose medium, back diluted to an optical density at 600 nm (OD_{600}) of 0.1 in a 10 ml of galactose medium and grown at 25 °C for 5 h to induce expression of both NLS and NES constructs. Cells were then resuspended in 10 ml of glucose medium at 100 µM MG132 and incubated for additional 15 min 25 °C and then switched to 37 °C for 30 min to ensure inclusion formation before cycloheximide (CHX) chase. Cells were then immobilized on concanavalin deltaT culture dish (Thermo Fisher Scientific), washed with pre-warmed glucose medium and incubated with glucose medium supplemented with 100 µM MG132 and 50 mg ml^{-1} of CHX. Images were taken every 25 s for 120 min at 37 °C as mentioned above.

FM4-64 vacuole labelling

Ten millilitres of cells were grown on galactose medium to a final OD_{600} of 0.8 at 25 °C. Vacuolar dye was added by resuspending the cells on 2 ml of fresh galactose medium plus FM4-64 to a final concentration of 8 µM, and incubated 30 min at 25 °C. For imaging, cells were then resuspended in glucose medium at 100 µM MG132 and incubated 20 min at 37 °C to induce inclusion formation. Cells were adhered on a concanavalin deltaT culture dish and imaged as mentioned above.

Immunostaining

As in the live-cell imaging assay, cells were grown overnight in raffinose medium followed by 4–6 h at 28 °C in galactose medium to induce the expression. Then, the cells were heat-shocked at 37 °C in glucose medium for 1 h before fixation in 4% paraformaldehyde for 15 min at 37 °C followed by methanol fixation for 20 min at −20 °C. Immunostaining proceeded as in ref. [109]. Briefly, samples were resuspended in sorbitol buffer and spheroplasted in Zymolyase for 30 min at room temperature and further solubilized in 0.1% Triton X-100 for 10 min. Antibodies are diluted in Buffer WT (1% non-fat dry milk, 0.5 mg ml^{-1} bovine serum albumin BSA, 200 mM NaCl, 50 mM HEPES–KOH (pH 7.5), 1 mM NaN_3 and 0.1% Tween-20) at a 1:500 dilution and incubated 2 h at room temperature or overnight at 4 °C. Samples are then washed in Buffer WT followed by incubation in secondary antibodies at a 1:1,000 dilution for 2 h at room temperature. Cells were immobilized on poly-lysine-coated coverslips and mounted in Prolong Diamond mounting medium (with DAPI where indicated) (Thermo Fisher). Nanobodies against EGFP and RFP were conjugated to Alexa Fluor 488 and Alexa Fluor 568, respectively, and used to amplify the signal from the fluorescent proteins during the SIM measurements. Anti-Nsp1 antibody from EnCor Biotechnology was used to visualize nuclear pores, and anti-Nsr1 antibody from Abcam was used for staining the nucleolus. Alternatively, we used the FluoTag-X4 anti-GFP Atto 488 and the FluoTag-X4 anti-RFP Atto 565 (NanoTag Technologies).

Confocal microscopy

Confocal microscopy on immunostained samples was performed on a Zeiss LSM700 inverted confocal microscope with 405, 488, 555 and 639 nm laser lines with Basic Filterset for LSM700 (Zeiss), a Plan-Apochromat 100×/1.4 oil DIC WD 0.17 objective (Zeiss) and a digital Axiocam MRm camera (Zeiss) controlled with the Zen black software. Confocal datasets were deconvolved when indicated using the Zen software with a fast-iterative function. Fluorescence was quantified where indicated using ImageJ software (National Institutes of Health (NIH)). The sGFP intensity measurements were performed as described previously[31]. Briefly, the raw integrated density (herein indicated as intensity) was measured for the nucleus and the whole cell. The intensity value of the nucleus was then divided by the area. The cytoplasmic intensity was calculated by subtracting the nuclear

intensity from the whole cell intensity and the cytoplasmic area by subtracting the nuclear area from the whole cell area. The cytoplasmic intensity was then divided by the cytoplasmic area. Finally, the ratio of cytoplasmic to nuclear was calculated by dividing the cytoplasmic intensity per area by the nuclear intensity per area. Statistical analysis was performed using Prism (GraphPad).

Super-resolution microscopy

SIM on immunostained samples was performed using an OMX V4 Blaze system (Applied Precision, GE Healthcare) equipped with a 100×/1.40 numerical aperture PlanApo oil-immersion objective (Olympus), 405, 488, 568 and 647 nm diode lasers with standard filter sets, and three emCCD cameras (Photometrics Evolve 512). SIM data were acquired with a *Z*-distance of 125 nm and with 15 images per plane (five phases and three angles). The raw data were computationally reconstructed using a Wiener (high-frequency) filter setting of between 0.001 and 0.003 and channel-specific optical transfer functions (OTFs) employing the softWoRx version 6.5.2 software package (GE Healthcare) to obtain a super-resolution image stack. 3D reconstructions and line intensity profiles were generated in Volocity version 6.3 (PerkinElmer).

To construct *NVJ1-sfGFP* strain with integrated sfGFP fusion at the C-terminal, sf*GFP* was knocked-in via standard polymerase chain reaction (PCR)-based homologous recombination. The *sfGFP* cassette was amplified from plasmid GTL-g (Addgene plasmid #81099) with oligonucleotides

5’TAGATGCACAAGTGAACACTGAACAAGCATACTCTCAACCATTTAGATACGCGGCCGCTCTAGAACTA and

5’TCGCACCTCGTTGTAAGTGACGATGATAACCGAGATGACGGAAATATAGTACA

ATGGAAAAACGCCAGCAACG. The cassette was amplified, separated by electrophoresis, gel purified and transformed into yeast cells using the lithium acetate method. Correct transformants were verified by standard PCR using the oligonucleotides NVJ1-VF: 5’GGATACCAGAACAACCTCTTC, NVJ1-VR: 5’ATGCCCGGCGTTATATATTGC and LEU2-VF: 5’AGCACGAGCCTCCTTTACCT.

Keima cloning

The NLS-Keima-luciTS plasmid was constructed by replacing the GFP oiety with yeast optimized Keima using a cassette amplified from plasmid pFA6a-link-yomKeima-Kan (Addgene plasmid #44902) with the oligonucleotides 5’ATGGCTTCTCCTAAGAAGAAACGTAAAGTTATGGTTTCTGTGATCGCTAAACAAATGAC and 5’CCATGCAAGCTTGCGCGGATCCGCGCCCTAATAGAGAATGTCTTGCGATAGC. Similarly, the NES-Keima-luciTS plasmid was created replacing the GFP moity using the oligonucleotides 5’CTCGCACTTAAGTTCGCCGGTTTAGACCTGATGGTTTCTGTGATCGCTAAACAAATGAC and 5’CCATGCAAGCTTGCGCGGATCCGCGCCCTAATAGAGAATGTCTTGCGATAGC. To construct the NLS and NES-2xKeima-luciTS, an additional Keima moiety was created by inserting a second keima cassette amplified using the oligonucleotides 5’CCATGCAAGCTTGCGCGGATCCGCGCCCTAATAGAGAATGTCTTGCGATAGC and 5’TTCCATGCAAGCTTGCGCGGATCCGCGCCCTAATAGAGAATGTCTTGCGA.

Live cell LeicaSp8/sSTED microscopy of Keima-tagged inclusions

Cells were grown as for time-resolved live fluorescence microscopy, adhered on concanavalin deltaT culture dish and examined at 37 °C for 90 min. Representative cells were collected every 5 min on a Leica TCS SP8 inverted sSTED microscope equipped with a 100×/1.40 APO (apochromatic objective) objective and using the following detection mirror settings: Keima 590–650 nm. Cells were sequentially excited using 404 nm (for acidic, excitation peak 440 nm) and 568 (for neutral, excitation peak 558 nm) laser lines respectively. One representative middle slide was acquired, and images were deconvolved and background subtracted using Huygens Professional (Scientific Volume Imaging).

X-ray tomography

Preparation of specimen mounting capillaries

Thin-walled glass capillaries were pulled as described in ref. [47]. After being cut to length, capillaries were dipped in poly-L-lysine (0.01% solution, tissue culture grade, Sigma-Aldrich). Fiducial markers, used to align soft X-ray projection images to a common axis, were generated by briefly immersing the capillaries a solution of 100 nm gold nanoparticles (EMGC100, BBI International), rinsing and then drying them in air.

Specimen capillaries for use in correlated imaging experiments were prepared as above and then dipped in a suspension of red polystyrene microspheres (FluoSpheres carboxylate-modified microspheres, 0.2 µm, dark red fluorescent (660 excitation/680 emission), Life Technologies, Invitrogen). The polystyrene microspheres were used fiducial markers for the alignment of fluorescence images to each other and for the co-alignment of soft X-ray and cryo-fluorescence tomographic reconstructions.

Specimen mounting

One millilitre of yeast cells in mid-log phase growth (OD_{600} ~0.5) was pelleted and resuspended in ~50 µl medium. One microlitre of this suspension was transferred into a specimen capillary using a standard micropipette. The capillary contents were immediately cryo-preserved by rapid plunging into liquid propane at 165 °C using a custom apparatus. Cryo-preserved specimens were transferred into storage boxes using a home-built cryo-transfer device and stored in a Dewar held at 77 K (ref. [47]).

Imaging cells in the cryogenic CLM

Specimen capillaries were transferred cryogenically to a home-built cryogenic spinning disk confocal fluorescence microscope[50]. Confocal scanning and detection were achieved using a commercial dual spinning disk head (CSU-X1, Yokogawa). During imaging, the illumination wavelength was selected with an acousto-optical tunable filter using an integrated system (Andor Laser Combiner, Model LC-501A).

Experimental measurement of the CLM PSF

The point spread function (PSF) of the cryogenic confocal light microscope (CLM) was calculated by the methods described in ref. [48].

Acquisition of cryogenic fluorescence tomography data

Cryo-preserved specimen capillaries were cryo-transferred to the CLM and aligned with respect to the rotation axis. Through-focus stacks or '*z*-stacks' were taken using a step size of 0.78 µm. For fluorescence tomography, the capillary was rotated about an axis normal to the objective lens using a motorized goniometer driven by custom LabView code (National Instruments Corporation). Each tomographic data series consisted of 37 through-focus stacks (0° through 360° measured at 10° increments). Once measurements were completed, the capillary was cryo-transferred back to liquid nitrogen storage using the cryo-transfer device[48].

Alignment of through-focus fluorescence stacks using fluorescence fiducials

Well-isolated fluorescent fiducials were chosen manually from the raw fluorescence stacks, and a three-dimensional centroid algorithm refined the bead position to subpixel accuracy using the software package Amira (FEI). The fiducial coordinates were used to write a new image stack in MATLAB containing a spherically symmetrical representation of the fiducials, which we termed the 'fiducial model'. Six parameters were optimized for each alignment: three translations and three rotations (a rigid affine transformation). By limiting the search space to optimize correspondence between bead pairs that had been visually verified to be true fiducial correspondences, this alignment strategy was relatively fast and robust. The entire fluorescence fiducial alignment optimization process was visualized in Amira. Visualization was helpful for inspecting the results and

troubleshooting rare cases where the optimization settled into a local maximum that was obviously not the real solution.

Fluorescence tomographic reconstruction and deconvolution

Pre-processed, aligned through-focus stacks were reconstructed into a single object by simply summing the through-focus datasets (Amira). The effective PSF for tomographic imaging in a specimen capillary was used as the convolution kernel to deconvolve the fluorescence reconstruction. We used an iterative function for the deconvolution. The algorithm found the fluorophore distribution that was most likely, assuming the PSF was spatially invariant and that image formation followed Poisson statistics.

Soft X-ray data collection and reconstruction

Specimens were imaged using a transmission soft X-ray microscope, operated by the National Center for X-ray Tomography (NCXT), at the Advanced Light Source of Lawrence Berkeley National Laboratory and reconstructed according to previously published protocols.

Correlated imaging

Co-alignment of cryogenic fluorescence and soft X-ray tomographic reconstructions using joint fiducials

Joint fiducials—red fluorescent polystyrene microspheres—visible in both light and soft X-ray images were used to guide overlay of the two data types. The alignment process was optimized by converting the raw fluorescence into a bead model and aligning the fluorescent bead model to the X-ray reconstruction of the beads using an iterative optimization of the overlay.

Identification of JUNQ/IPOD in soft X-ray reconstructions

Segmentation is the process of computationally isolating, visualizing and quantifying specific cellular components in a tomographic reconstruction. Each voxel in an SXT reconstruction is a direct measurement of the soft X-ray LAC at the corresponding location in the cell. Attenuation of the illumination by the specimen follows Beer's law. Hence, the LAC values for identically sized voxels depend solely on the concentration and composition of biomolecules present. Consequently, water has an order-of-magnitude-lower LAC than carbon-containing molecules, such as lipids and proteins. LAC values for homogeneous solutions of isolated biomolecules can also be calculated using tables of known absorption coefficients. For example, pure water in the form of ice has a calculated LAC of 0.109 μm^{-1}, whereas a model protein with the chemical composition $C_{94}H_{139}N_{24}O_{31}S$ was calculated to have a theoretical LAC of 1.35 μm^{-1}(ref. [110]). In practice, most of the voxels in a 50 nm resolution SXT reconstruction of a cell will contain a heterogeneous mixture of biomolecules. Using SXT data acquired at a single wavelength it is not possible to distinguish the precise chemical species present. However, at this level of spatial resolution organelles and other subcellular structures are sufficiently similar in their biochemical composition to allow them to be readily identified from the surrounding cell contents. The relatively high water content in vacuoles makes them readily distinguishable from organelles with a greater density of biomolecules, for example, nuclei and mitochondria. Even relatively small variations in organelle LAC can be distinguished, for example, the boundaries between nuclei and nucleoli are very clear, as is the distinction between euchromatin and heterochromatin domains in the nucleus. LACs were calculated, and cells segmented using the protocols are described in complete detail in ref. [47].

Segmentation of the Hsp104-GFP reconstructions, in particular the assignment of the volumes as JUNQ and IPOD, were guided by correlative fluorescence signal. In other strains, JUNQ and/or IPOD were assigned on the basis of LAC values established in the Hsp104-GFP study.

Western blot

Yeast cultures were grown to mid-log phase in synthetic complete medium (yeast nitrogen base, ammonium sulfate, amino acids and 2% raffinose) lacking uracil. Cultures were then diluted to an OD_{600} of 0.2 in galactose medium (synthetic complete medium with 2% galactose and 2% raffinose) and grown to an OD_{600} of 0.8. Cultures were then pelleted and resuspended in glucose medium (synthetic complete medium with 2% glucose) and incubated at either 30 °C or 37 °C as indicated for the duration of the shut off. Where indicated, cultures were shifted to 37 °C for 1 h before exchange into glucose medium and incubated at 37 °C for the duration of the glucose shut-off. Cells were pelleted, proteins were extracted with urea and sodium dodecyl sulfate, and protein concentrations were measured with the bicinchoninic acid protein assay kit (Thermo Fisher Scientific). Equal amounts of total protein were resolved on Tris–glycine gels (Invitrogen) and transferred onto nitrocellulose membranes. EGFP was detected with mouse anti-GFP antibodies (Roche), GAPDH was detected with rabbit anti-GAPHD (Genetex) and PGK was detected with rabbit anti-PGK antibody (Thermo Fisher Scientific). Secondary antibodies were IRDye 800CW donkey anti-mouse or IRDye 680RD donkey anti-rabbit and were imaged using the LiCOR scanner and Image Studio software.

To assess vacuolar protein degradation, the same procedure as above was followed but the *pep4D* yeast was treated with 1 mM PMSF (Research Products International) during the 37 °C incubation step. The samples were then collected and lysed as above. EGFP and GAPDH were detected with the same primary antibodies, but the secondary antibodies were goat anti-mouse HRP conjugated antibody (Promega cat. no. W4021) and goat anti-rabbit HRP conjugated antibody (Promega cat. no. W4011). Blots were detected using Clarity Western ECL Substrate (Bio-Rad cat. no. 1705061) and imaged using the GE Amersham Imager 600 and control software version 1.2.0.

Drop test

Yeast cultures were grown to OD_{600} of 0.6 in YPD or raffinose synthetic complete medium and then diluted to OD_{600} of 0.1. Four ten-fold serial dilutions were performed in H_2O. Approximately 2 µl of diluted cultures were spotted onto YPD, galactose or glucose plates using the pin plater. Plates were incubated at indicated temperatures and imaged every 24 h for 72 h.

Nanobody purification and labelling

GFP nanobody was expressed in BL21 Rosetta2 pLysS cells (Novagen), and DsRed nanobody (LAM4) was expressed in ArticExpress cells (Agilent Technologies) overnight at 17 °C and 12 °C, respectively. Cells were pelleted (4,000*g*), washed with PBS containing 1 mM PMSF and pelleted again. Pellets were resuspended in column buffer (500 mM NaCl and 50 mM HEPES pH 8 or 50 mM $NaHCO_3$ pH 8.3) with complete protease inhibitors, PMSF, benzonase and 10 mM imidazole (Lysis buffer) and lysed using an emulsiflex. Lysates were cleared at 20,000*g* for 30 min. Nanobodies were purified using nickel resin by passing cleared lysate over the resin, washing with lysis buffer, followed by column buffer, and elution with column buffer containing 300 mM imidazole. Elution was concentrated using an Amicon Ultra 3 kD MWCO to less than 2 ml, and further purified by size exclusion using an SDX75 column (GE Healthcare) equilibrated with 500 mM NaCl, 50 mM $NaHCO_3$ and 1 mM dithiothreitol. Labelling was performed by the addition of dyes at a molar ratio of 5:1 dye:nanobody using Alexa 488 NHS (Thermo Fisher Scientific) for the GFP nanobody and Alexa 568 NHS (Thermo Fisher Scientific) for the DsRed nanobody. Labelling reactions were incubated 1 h at room temperature and quenched by addition of Tris–HCl pH 8 to a final concentration of 100 mM. Labelled nanobody was separated from free dye by size exclusion using an SDX75 column.

GFP-nanobody cloning

pDG402, a vector for expression of GFP-nanobody-TEV-6Xhis was generated by PCR amplification of the GFP nanobody using the 5' primer (XbaI GFP nanobody) AATCTAGAATTTTGTTTAACTTTAAGAAGG and 3' primer (GS link TEV His nanobody) AAGGATCCTTATCAGTGATGATGGTGGTGATGGGACCCAGATCCACCCTGGAAGTATAAATTCTCACCCGAACCTCCGGATGAGGAGACGGTGACCTGGG. The PCR product was cloned into the pST39 backbone111 using XbaI and BamHI.

Yeast strains and plasmids

The yeast strains and plasmids used in this study are available in the supplementary table.

Statistics and reproducibility

Puncta counting

A power analysis was performed (StatMate v1.0, GraphPad) on data from a pilot experiment to determine the relevant number of cells to count for each experiment to achieve 95% power. Images were taken at random locations on a coverslip to achieve the desired number of cells for 95% power. Images were saved with a non-identifying file name and quantitated by a researcher blinded to the group. File names were decoded, and data were entered into Prism (GraphPad v5.04 and 9) for further statistical analyses as described below. No data were excluded from the analyses.

Microscopy

Microscopy images are representative of three independent experiments unless otherwise specified in the figure legend. Images were taken at random locations on a coverslip. Images were saved with a non-identifying file name and quantitated by a researcher blinded to the group.

Ratio of cytoplasmic:nuclear fluorescence in Fig. **2d**

Kruskal–Wallis test with Dunn's multiple comparisons test was performed using Prism. Adjusted *P* value of no treatment versus MG132 is 0.0014, no treatment versus 97QΔP is 0.0027 and no treatment versus LMB is <0.0001. Twenty cells per condition from five biologically independent experiments were normalized to the no treatment control, analysed and presented as violin plots with median values shown as dashed lines and quartile values shown as dotted lines. No data were excluded from the analyses.

Nvj1Δ puncta counting in Fig. **5h**

A minimum of 500 cells per condition from three biologically independent experiments were counted, and two-tailed unpaired Student's *t*-tests were performed comparing the deletion strains to WT. *P* values were adjusted using two-stage linear step-up procedure of Benjamini, Krieger and Yekutieli with a false discovery rate (*Q*) of 5%. Adjusted *P* value for NLS-LuciTs: WT versus *nvj1Δ* is 0.0205, and WT versus *vac8Δ* is 0.0406. Adjusted *P* value for NES-LuciTs: WT versus *nvj1Δ* is 0.013, and WT versus *vac8Δ* is 0.0008. No data were excluded from the analyses.

vps4Δ puncta counting in Fig. **6e**

A minimum of 100 cells per condition from four biologically independent experiments were counted, and two-tailed Student's *t*-tests were performed comparing the deletion strains to WT. *P* value for WT versus *vps4Δ* NLS-LuciTs is 0.0007, and WT versus *vps4Δ* NES-LuciTs is 0.0018. No data were excluded from the analyses.

Puncta counting in Extended Data Fig. 5c,d

A minimum of 500 cells per condition from three biologically independent experiments were counted, and two-tailed unpaired Student's *t*-tests were performed comparing the deletion strains to WT with or without MG132 treatment. *P* values were adjusted using two-stage linear step-up procedure of Benjamini, Krieger and Yekutieli

with a *Q* of 5%. Data are shown as mean ± standard error of the mean (s.e.m.). Panel c shows adjusted *P* value for WT versus *nvj1*Δ no MG132 is 0.0205, WT versus *nvj1*Δ + MG132 is 0.2357, WT versus *vac8Δ* no MG132 is 0.0406, WT versus *vac8*Δ + MG132 is 0.8974 and WT no MG132 versus WT + MG132 is 0.0239. In panel d, adjusted *P* value for WT versus *nvj1*Δ no MG132 is 0.013, WT versus *nvj1*Δ + MG132 is 0.013, WT versus *vac8*Δ no MG132 is 0.0008, WT versus *vac8*Δ + MG132 is 0.0447 and WT no MG132 versus WT + MG132 is 0.0005. In panel e, levels of EGFP after 1 h at 37 °C were measured from quantitative western blots (mean ± s.e.m. from three biologically independent experiments). WT and nvj1Δ yeast were compared using a two-tailed unpaired Student's *t*-test resulting in a *P* value of 0.0043 for WT versus nvj1Δ NLS-LuciTs, and NES-LuciTs *P* value is 0.0183. Statistics were performed using Prism.

Reporting summary

Further information on research design is available in the Nature Portfolio Reporting Summary linked to this article.

Data availability

Source data are provided with this paper. All other data that support the findings of this study are available from J.F. upon reasonable request.

References

1. Hartl, F. U., Bracher, A. & Hayer-Hartl, M. Molecular chaperones in protein folding and proteostasis. *Nature* **475**, 324–332 (2011).
2. Needham, P. G., Guerriero, C. J. & Brodsky, J. L. Chaperoning endoplasmic reticulum-associated degradation (ERAD) and protein conformational diseases. *Cold Spring Harb. Perspect. Biol.* **11**, a033928 (2019).
3. Balchin, D., Hayer-Hartl, M. & Hartl, F. U. In vivo aspects of protein folding and quality control. *Science* **353**, aac4354 (2016).
4. Sontag, E. M., Samant, R. S. & Frydman, J. Mechanisms and functions of spatial protein quality control. *Annu. Rev. Biochem.* **20**, 97–122 (2017).
5. Pohl, C. & Dikic, I. Cellular quality control by the ubiquitin–proteasome system and autophagy. *Science* **366**, 818–822 (2019).
6. Finley, D. & Prado, M. A. The proteasome and its network: engineering for adaptability. *Cold Spring Harb. Perspect. Biol.* **12**, a033985 (2020).
7. Alberti, S. & Hyman, A. A. Are aberrant phase transitions a driver of cellular aging? *BioEssays* **38**, 959–968 (2016).
8. Ano Bom, A. P. et al. Mutant p53 aggregates into prion-like amyloid oligomers and fibrils: implications for cancer. *J. Biol. Chem.* **287**, 28152–28162 (2012).
9. Douglas, P. M. & Dillin, A. Protein homeostasis and aging in neurodegeneration. *J. Cell Biol.* **190**, 719–729 (2010).
10. De Mattos, E. P. et al. Protein quality control pathways at the crossroad of synucleinopathies. *J. Parkinsons Dis.* **10**, 369–382 (2020).
11. Kaganovich, D., Kopito, R. & Frydman, J. Misfolded proteins partition between two distinct quality control compartments. *Nature* **454**, 1088–1095 (2008).
12. Dillin, A. & Cohen, E. Ageing and protein aggregation-mediated disorders: from invertebrates to mammals. *Philos. Trans. R. Soc. Lond. B Biol. Sci.* **366**, 94–98 (2011).
13. Balch, W. E., Morimoto, R. I., Dillin, A. & Kelly, J. W. Adapting proteostasis for disease intervention. *Science* **319**, 916–919 (2008).

14. Reichmann, D., Voth, W. & Jakob, U. Maintaining a healthy proteome during oxidative stress. *Mol. Cell* **69**, 203–213 (2018).
15. Morales-Polanco, F., Lee, J. H., Barbosa, N. M. & Frydman, J. Cotranslational mechanisms of protein biogenesis and complex assembly in eukaryotes. *Annu. Rev. Biomed. Data Sci.* **5**, 67–94 (2022).
16. Specht, S., Miller, S. B., Mogk, A. & Bukau, B. Hsp42 is required for sequestration of protein aggregates into deposition sites in *Saccharomyces cerevisiae*. *J. Cell Biol.* **195**, 617–629 (2011).
17. Escusa-Toret, S., Vonk, W. I. & Frydman, J. Spatial sequestration of misfolded proteins by a dynamic chaperone pathway enhances cellular fitness during stress. *Nat. Cell Biol.* https://doi.org/10.1038/ncb2838 (2013).
18. Miller, S. B. et al. Compartment-specific aggregases direct distinct nuclear and cytoplasmic aggregate deposition. *EMBO J.* **34**, 778–797 (2015).
19. Weisberg, S. J. et al. Compartmentalization of superoxide dismutase 1 (SOD1G93A) aggregates determines their toxicity. *Proc. Natl Acad. Sci. USA* **109**, 15811–15816 (2012).
20. Babazadeh, R. et al. Syntaxin 5 is required for the formation and clearance of protein inclusions during proteostatic stress. *Cell Rep.* **28**, 2096–2110 (2019).
21. Nollen, E. A. et al. Dynamic changes in the localization of thermally unfolded nuclear proteins associated with chaperone-dependent protection. *Proc. Natl Acad. Sci. USA* **98**, 12038–12043 (2001).
22. Yasuda, S. et al. Stress- and ubiquitylation-dependent phase separation of the proteasome. *Nature* **578**, 296–300 (2020).
23. Polling, S. et al. Misfolded polyglutamine, polyalanine, and superoxide dismutase 1 aggregate via distinct pathways in the cell. *J. Biol. Chem.* **289**, 6669–6680 (2014).
24. Park, J. H. et al. Amyotrophic lateral sclerosis-related mutant superoxide dismutase 1 aggregates inhibit 14-3-3-mediated cell survival by sequestration into the JUNQ compartment. *Hum. Mol. Genet.* **26**, 3615–3629 (2017).
25. Samant, R. S., Livingston, C. M., Sontag, E. M. & Frydman, J. Distinct proteostasis circuits cooperate in nuclear and cytoplasmic protein quality control. *Nature* **563**, 407–411 (2018).
26. McClellan, A. J., Scott, M. D. & Frydman, J. Folding and quality control of the VHL tumor suppressor proceed through distinct chaperone pathways. *Cell* **121**, 739–748 (2005).
27. Gupta, R. et al. Firefly luciferase mutants as sensors of proteome stress. *Nat. Methods* **8**, 879–884 (2011).
28. Popken, P., Ghavami, A., Onck, P. R., Poolman, B. & Veenhoff, L. M. Size-dependent leak of soluble and membrane proteins through the yeast nuclear pore complex. *Mol. Biol. Cell* **26**, 1386–1394 (2015).
29. Amm, I. & Wolf, D. H. Molecular mass as a determinant for nuclear San1-dependent targeting of misfolded cytosolic proteins to proteasomal degradation. *FEBS Lett.* **590**, 1765–1775 (2016).
30. Timney, B. L. et al. Simple rules for passive diffusion through the nuclear pore complex. *J. Cell Biol.* **215**, 57–76 (2016).
31. Woerner, A. C. et al. Cytoplasmic protein aggregates interfere with nucleocytoplasmic transport of protein and RNA. *Science* **351**, 173–176 (2016).
32. Park, S. H. et al. PolyQ proteins interfere with nuclear degradation of cytosolic proteins by sequestering the Sis1p Chaperone. *Cell* **154**, 134–145 (2013).
33. Neuber, A. et al. Nuclear export receptor Xpo1/Crm1 is physically and functionally linked to the spindle pole body in budding yeast. *Mol. Cell. Biol.* **28**, 5348–5358 (2008).
34. Grima, J. C. et al. Mutant huntingtin disrupts the nuclear pore complex. *Neuron* **94**, 93–107 (2017).
35. Gasset-Rosa, F. et al. Polyglutamine-expanded huntingtin exacerbates age-related disruption of nuclear integrity and nucleocytoplasmic transport. *Neuron* **94**, 48–57 (2017).

36. Wente, S. R. & Blobel, G. A temperature-sensitive NUP116 null mutant forms a nuclear envelope seal over the yeast nuclear pore complex thereby blocking nucleocytoplasmic traffic. *J. Cell Biol.* **123**, 275–284 (1993).
37. Chen, L. et al. Sts1 plays a key role in targeting proteasomes to the nucleus. *J. Biol. Chem.* **286**, 3104–3118 (2011).
38. Takeda, K. & Yanagida, M. Regulation of nuclear proteasome by Rhp6/Ubc2 through ubiquitination and destruction of the sensor and anchor Cut8. *Cell* **122**, 393–405 (2005).
39. Tatebe, H. & Yanagida, M. Cut8, essential for anaphase, controls localization of 26S proteasome, facilitating destruction of cyclin and Cut2. *Curr. Biol.* **10**, 1329–1338 (2000).
40. Romero-Perez, L., Chen, L., Lambertson, D. & Madura, K. Sts1 can overcome the loss of Rad23 and Rpn10 and represents a novel regulator of the ubiquitin/proteasome pathway. *J. Biol. Chem.* **282**, 35574–35582 (2007).
41. Lord, C. L. & Wente, S. R. Nuclear envelope–vacuole contacts mitigate nuclear pore complex assembly stress. *J. Cell Biol.* **219**, e202001165 (2020).
42. Crisp, M. et al. Coupling of the nucleus and cytoplasm: role of the LINC complex. *J. Cell Biol.* **172**, 41–53 (2006).
43. Aitchison, J. D., Blobel, G. & Rout, M. P. Nup120p: a yeast nucleoporin required for NPC distribution and mRNA transport. *J. Cell Biol.* **131**, 1659–1675 (1995).
44. Heath, C. V. et al. Nuclear pore complex clustering and nuclear accumulation of poly(A)+ RNA associated with mutation of the *Saccharomyces cerevisiae* RAT2/NUP120 gene. *J. Cell Biol.* **131**, 1677–1697 (1995).
45. Ader, C. et al. Amyloid-like interactions within nucleoporin FG hydrogels. *Proc. Natl Acad. Sci. USA* **107**, 6281–6285 (2010).
46. Strawn, L. A., Shen, T., Shulga, N., Goldfarb, D. S. & Wente, S. R. Minimal nuclear pore complexes define FG repeat domains essential for transport. *Nat. Cell Biol.* **6**, 197–206 (2004).
47. Parkinson, D. Y. et al. Nanoimaging cells using soft X-ray tomography. *Methods Mol. Biol.* **950**, 457–481 (2013).
48. Le Gros, M. A. et al. Biological soft X-ray tomography on beamline 2.1 at the Advanced Light Source. *J. Synchrotron Radiat.* **21**, 1370–1377 (2014).
49. Larabell, C. A. & Nugent, K. A. Imaging cellular architecture with X-rays. *Curr. Opin. Struct. Biol.* **20**, 623–631 (2010).
50. Le Gros, M. A., McDermott, G., Uchida, M., Knoechel, C. G. & Larabell, C. A. High-aperture cryogenic light microscopy. *J. Microsc.* **235**, 1–8 (2009).
51. Ekman, A. et al. in *Synchrotron Light Sources and Free-Electron Lasers: Accelerator Physics, Instrumentation and Science Applications* (eds Jaeschke, E. et al.) 1–32 (Springer International Publishing, 2019).
52. Ekman, A. A. et al. Mesoscale imaging with cryo-light and X-rays: larger than molecular machines, smaller than a cell. *Biol. Cell* **109**, 24–38 (2017).
53. Huh, W. K. et al. Global analysis of protein localization in budding yeast. *Nature* **425**, 686–691 (2003).
54. Wu, G. H. et al. Multi-scale 3D cryo-correlative microscopy for vitrified cells. *Structure* **28**, 1231–1237 (2020).
55. Schuler, M. H. et al. Miro1-mediated mitochondrial positioning shapes intracellular energy gradients required for cell migration. *Mol. Biol. Cell* **28**, 2159–2169 (2017).
56. Frottin, F. et al. The nucleolus functions as a phase-separated protein quality control compartment. *Science* **365**, 342–347 (2019).
57. Velazquez, J. M. & Lindquist, S. hsp70: nuclear concentration during environmental stress and cytoplasmic storage during recovery. *Cell* **36**, 655–662 (1984).

58. Falahati, H., Pelham-Webb, B., Blythe, S. & Wieschaus, E. Nucleation by rRNA dictates the precision of nucleolus assembly. *Curr. Biol.* **26**, 277–285 (2016).
59. Azkanaz, M. et al. Protein quality control in the nucleolus safeguards recovery of epigenetic regulators after heat shock. *eLife* **8**, e45205 (2019).
60. Pan, X. et al. Nucleus–vacuole junctions in *Saccharomyces cerevisiae* are formed through the direct interaction of Vac8p with Nvj1p. *Mol. Biol. Cell* **11**, 2445–2457 (2000).
61. Kohlwein, S. D. et al. Tsc13p is required for fatty acid elongation and localizes to a novel structure at the nuclear–vacuolar interface in *Saccharomyces cerevisiae*. *Mol. Cell. Biol.* **21**, 109–125 (2001).
62. Levine, T. P. & Munro, S. Dual targeting of Osh1p, a yeast homologue of oxysterol-binding protein, to both the Golgi and the nucleus–vacuole junction. *Mol. Biol. Cell* **12**, 1633–1644 (2001).
63. Kvam, E. & Goldfarb, D. S. Structure and function of nucleus–vacuole junctions: outer-nuclear-membrane targeting of Nvj1p and a role in tryptophan uptake. *J. Cell Sci.* **119**, 3622–3633 (2006).
64. Kvam, E. & Goldfarb, D. S. Nucleus–vacuole junctions and piecemeal microautophagy of the nucleus in *S. cerevisiae*. *Autophagy* **3**, 85–92 (2007).
65. Roberts, P. et al. Piecemeal microautophagy of nucleus in *Saccharomyces cerevisiae*. *Mol. Biol. Cell* **14**, 129–141 (2003).
66. Krick, R. et al. Piecemeal microautophagy of the nucleus requires the core macroautophagy genes. *Mol. Biol. Cell* **19**, 4492–4505 (2008).
67. von Knebel Doeberitz, M. & Wentzensen, N. in *Comprehensive Cytopathology* 3rd edn, (eds Bibbo, M. & Wilbur D.) Ch. 1 (Saunders, 2008).
68. Ponsford, A. H. et al. Live imaging of intra-lysosome pH in cell lines and primary neuronal culture using a novel genetically encoded biosensor. *Autophagy* **17**, 1500–1518 (2021).
69. Campbell, T. N. & Choy, F. Y. M. The effect of pH on green fluorescent protein: a brief review. *Mol. Biol. Today* **2**, 1–4 (2001).
70. Tsien, R. Y. The green fluorescent protein. *Annu. Rev. Biochem.* **67**, 509–544 (1998).
71. Haupts, U., Maiti, S., Schwille, P. & Webb, W. W. Dynamics of fluorescence fluctuations in green fluorescent protein observed by fluorescence correlation spectroscopy. *Proc. Natl Acad. Sci. USA* **95**, 13573–13578 (1998).
72. Ho, C. Y., Choy, C. H., Wattson, C. A., Johnson, D. E. & Botelho, R. J. The Fab1/PIKfyve phosphoinositide phosphate kinase is not necessary to maintain the pH of lysosomes and of the yeast vacuole. *J. Biol. Chem.* **290**, 9919–9928 (2015).
73. Cormack, B. P., Valdivia, R. H. & Falkow, S. FACS-optimized mutants of the green fluorescent protein (GFP). *Gene* **173**, 33–38 (1996).
74. von Appen, A. et al. LEM2 phase separation promotes ESCRT-mediated nuclear envelope reformation. *Nature* **582**, 115–118 (2020).
75. Thaller, D. J. & Patrick Lusk, C. Fantastic nuclear envelope herniations and where to find them. *Biochem. Soc. Trans.* **46**, 877–889 (2018).
76. Webster, B. M. et al. Chm7 and Heh1 collaborate to link nuclear pore complex quality control with nuclear envelope sealing. *EMBO J.* **35**, 2447–2467 (2016).
77. Thaller, D. J. et al. An ESCRT-LEM protein surveillance system is poised to directly monitor the nuclear envelope and nuclear transport system. *eLife* **8**, e45284 (2019).
78. Babst, M., Odorizzi, G., Estepa, E. J. & Emr, S. D. Mammalian tumor susceptibility gene 101 (TSG101) and the yeast homologue, Vps23p, both function in late endosomal trafficking. *Traffic* **1**, 248–258 (2000).
79. Katzmann, D. J., Babst, M. & Emr, S. D. Ubiquitin-dependent sorting into the multivesicular body pathway requires the function of a conserved endosomal protein sorting complex, ESCRT-I. *Cell* **106**, 145–155 (2001).

80. Herrador, A., Léon, S., Haguenauer-Tsapis, R. & Vincent, O. A mechanism for protein monoubiquitination dependent on a *trans*-acting ubiquitin-binding domain. *J. Biol. Chem.* **288**, 16206–16211 (2013).
81. Stack, J. H., Herman, P. K., Schu, P. V. & Emr, S. D. A membrane-associated complex containing the Vps15 protein kinase and the Vps34 PI 3-kinase is essential for protein sorting to the yeast lysosome-like vacuole. *EMBO J.* **12**, 2195–2204 (1993).
82. Herman, P. K. & Emr, S. D. Characterization of VPS34, a gene required for vacuolar protein sorting and vacuole segregation in *Saccharomyces cerevisiae*. *Mol. Cell. Biol.* **10**, 6742–6754 (1990).
83. Burda, P., Padilla, S. M., Sarkar, S. & Emr, S. D. Retromer function in endosome-to-Golgi retrograde transport is regulated by the yeast Vps34 PtdIns 3-kinase. *J. Cell Sci.* **115**, 3889–3900 (2002).
84. Slessareva, J. E., Routt, S. M., Temple, B., Bankaitis, V. A. & Dohlman, H. G. Activation of the phosphatidylinositol 3-kinase Vps34 by a G protein alpha subunit at the endosome. *Cell* **126**, 191–203 (2006).
85. Henne, W. M., Stenmark, H. & Emr, S. D. Molecular mechanisms of the membrane sculpting ESCRT pathway. *Cold Spring Harb. Perspect. Biol.* **5**, a016766 (2013).
86. Hurley, J. H. & Hanson, P. I. Membrane budding and scission by the ESCRT machinery: it's all in the neck. *Nat. Rev. Mol. Cell Biol.* **11**, 556–566 (2010).
87. Katayama, H., Kogure, T., Mizushima, N., Yoshimori, T. & Miyawaki, A. A sensitive and quantitative technique for detecting autophagic events based on lysosomal delivery. *Chem. Biol.* **18**, 1042–1052 (2011).
88. Bialecka-Fornal, M., Makushok, T. & Rafelski, S. M. A review of fluorescent proteins for use in yeast. *Methods Mol. Biol.* **1369**, 309–346 (2016).
89. Sitron, C. S., Park, J. H., Giafaglione, J. M. & Brandman, O. Aggregation of CAT tails blocks their degradation and causes proteotoxicity in *S. cerevisiae*. *PLoS ONE* **15**, e0227841 (2020).
90. Schuck, S., Gallagher, C. M. & Walter, P. ER-phagy mediates selective degradation of endoplasmic reticulum independently of the core autophagy machinery. *J. Cell Sci.* **127**, 4078–4088 (2014).
91. Klionsky, D. J. et al. Guidelines for the use and interpretation of assays for monitoring autophagy (4th edn). *Autophagy* **17**, 1–382 (2021).
92. Eising, S. et al. A lysosomal biogenesis map reveals the cargo spectrum of yeast vacuolar protein targeting pathways. *J. Cell Biol.* **221**, e202107148 (2022).
93. Waite, K. A., De-La Mota-Peynado, A., Vontz, G. & Roelofs, J. Starvation induces proteasome autophagy with different pathways for core and regulatory particles. *J. Biol. Chem.* **291**, 3239–3253 (2016).
94. Kvam, E. & Goldfarb, D. S. Nvj1p is the outer-nuclear-membrane receptor for oxysterol-binding protein homolog Osh1p in *Saccharomyces cerevisiae*. *J. Cell Sci.* **117**, 4959–4968 (2004).
95. Shinoda, H., Shannon, M. & Nagai, T. Fluorescent proteins for investigating biological events in acidic environments. *Int. J. Mol. Sci.* **19**, 1548 (2018).
96. Vida, T. A. & Emr, S. D. A new vital stain for visualizing vacuolar membrane dynamics and endocytosis in yeast. *J. Cell Biol.* **128**, 779–792 (1995).
97. Thorn, K. Genetically encoded fluorescent tags. *Mol. Biol. Cell* **28**, 848–857 (2017).
98. Costantini, L. M. et al. A palette of fluorescent proteins optimized for diverse cellular environments. *Nat. Commun.* **6**, 7670 (2015).
99. Amm, I., Sommer, T. & Wolf, D. H. Protein quality control and elimination of protein waste: the role of the ubiquitin–proteasome system. *Biochim. Biophys. Acta* **1843**, 182–196 (2014).
100. Eisele, F. et al. An Hsp90 co-chaperone links protein folding and degradation and is part of a conserved protein quality control. *Cell Rep.* **35**, 109328 (2021).
101. Arrasate, M., Mitra, S., Schweitzer, E. S., Segal, M. R. & Finkbeiner, S. Inclusion body formation reduces levels of mutant huntingtin and the risk of neuronal death. *Nature* **431**, 805–810 (2004).

102. Schneider, K. L. et al. Using reporters of different misfolded proteins reveals differential strategies in processing protein aggregates. *J. Biol. Chem.* **298**, 102476 (2022).
103. Kumar, B. et al. ESCRT-I protein Tsg101 plays a role in the post-macropinocytic trafficking and infection of endothelial cells by Kaposi's sarcoma-associated herpesvirus. *PLoS Pathog.* **12**, e1005960 (2016).
104. Gottschling, D. E. & Nystrom, T. The upsides and downsides of organelle interconnectivity. *Cell* **169**, 24–34 (2017).
105. Zhang, K. et al. The C9orf72 repeat expansion disrupts nucleocytoplasmic transport. *Nature* **525**, 56–61 (2015).
106. Fallini, C., Khalil, B., Smith, C. L. & Rossoll, W. Traffic jam at the nuclear pore: all roads lead to nucleocytoplasmic transport defects in ALS/FTD. *Neurobiol. Dis.* **140**, 104835 (2020).
107. Shang, J. et al. Aberrant distributions of nuclear pore complex proteins in ALS mice and ALS patients. *Neuroscience* **350**, 158–168 (2017).
108. Chou, C. C. et al. TDP-43 pathology disrupts nuclear pore complexes and nucleocytoplasmic transport in ALS/FTD. *Nat. Neurosci.* **21**, 228–239 (2018).
109. Brickner, D. G., Light, W. & Brickner, J. H. Quantitative localization of chromosomal loci by immunofluorescence. *Methods Enzymol.* **470**, 569–580 (2010).
110. Weiss, D. et al. Computed tomography of cryogenic biological specimens based on X-ray microscopic images. *Ultramicroscopy* **84**, 185–197 (2000).
111. Tan, S. A modular polycistronic expression system for overexpressing protein complexes in *Escherichia coli*. *Protein Expr. Purif.* **21**, 224–234 (2001).

Acknowledgements

Funded by NIH (GM05643319 and AG054407 to J.F.; F32NS086253 to E.M.S.); Way Klingler Startup Funds from Marquette University (E.M.S.); The Pew Trusts postdoctoral Award 00034104 to F.M.-P. and Gordon and Betty Moore Foundation Award #3497 to C.L. and M.A.L.G. Cryo-SXT data were acquired at National Center for X-ray Tomography (NIH P41GM103445and DOE DE-AC02-5CH11231). We thank J. Mulholland and Y. Lim from the CSIF for training on the SIM and M. Rosbash (Brandeis University), S. Wente (Vanderbilt University), K. Madura (Rutgers University) and P. Lusk (Yale School of Medicine) for yeast strains and K. Weis (ETH Zurich), J. Nunnari (University of California, Davis) and M. P. Rout (Rockefeller University) for plasmids. We are grateful to C. Trail for support in microscopy data analysis and M. Wangeline (Stanford University) for assisting with the 2xKeima cloning. We thank K. Ullman (University of Utah), A. Frost (Altos Lab), J. Steffan (UC Irvine) and L. Veenhoff (University of Groningen) for discussions and advice, F. Serrano for assisting on model figure and the Frydman lab for advice and discussions.

Author information

Author notes

Emily M. Sontag
Present address: Department of Biological Sciences, Marquette University, Milwaukee, WI, USA

Patrick T. Dolan
Present address: Quantitative Virology and Evolution Unit, National Institute of Allergy and Infectious Diseases, Bethesda, MD, USA

These authors contributed equally: Emily M. Sontag, Fabián Morales-Polanco.

Authors and Affiliations

Department of Biology, Stanford University, Stanford, CA, USA
Emily M. Sontag, Fabián Morales-Polanco, Patrick T. Dolan, Daniel Gestaut & Judith Frydman

Department of Anatomy, School of Medicine, University of California San Francisco, San Francisco, CA, USA
Jian-Hua Chen, Gerry McDermott, Mark A. Le Gros & Carolyn Larabell

Molecular Biophysics and Integrated Bioimaging Division, Lawrence Berkeley National Laboratory, Berkeley, CA, USA

Mark A. Le Gros & Carolyn Larabell

Contributions

E.M.S., F.M.-P. and J.F. designed all experiments. E.M.S. and F.M.-P. carried out all experiments. J.-H.C. collected and processed cryo-SXT data; C.L. assisted with planning and execution of cryo-SXT experiments; G.M. carried out cryo-SXT data analysis and modelling; M.A.L.G. performed cryo-fluorescence data acquisition and correlation with cryo-SXT data and built the microscope used for these experiments. P.T.D. analysed particle tracking data and assisted on statistical analyses. D.G. cloned the NLS- and NES-luciferase and VHL plasmids. F.M.-P. and D.G. generated, purified and labelled the GFP and RFP nanobodies. E.M.S., F.M.-P. and J.F. wrote the manuscript. All authors commented on the final version. J.F. and E.M.S. conceived the project; J.F. directed the project.

Corresponding authors

Correspondence to Emily M. Sontag or Judith Frydman.

Ethics declarations

Competing interests

The authors declare no competing interests.

Peer review

Peer review information

Nature Cell Biology thanks the anonymous reviewers for their contribution to the peer review of this work.

Additional information

Extended data

Extended Data Fig. 1 Spatial sequestration occurs during different types of stress with different client proteins.

(a) Western blot analyses of Gal Shut-off assays showing the clearance of NLS-LuciTs (top) and NES-LuciTs (bottom) with and without proteasome impairment by 50μM Bortezomib. Blot is representative of 3 biologically independent experiments. (b-c) Representative Structured Illumination super-resolution microscopy images taken of cells expressing NLS-VHL **(b)** or NES-VHL **(c)** after 120 minutes at 37 °C and treated with 100μM MG132. NLS-LuciTs is shown in green, NES-LuciTs in purple, nuclear pores in gold and Hoechst counterstain in blue. Scale

bars are 1µm. **(d)** Drop test of W303 yeast expressing model proteins without heat shock at 30C (left), with heat shock at 37 °C (middle), and without expression of the plasmids (right). Unprocessed blots are available in source data.

Extended Data Fig. 2 The effect of blocking nucleocytoplasmic transport on Ubc9Ts clearance.

(a) Quantitation of the percentage of cells containing nuclear or cytoplasmic inclusions in WT yeast expressing Ubc9Ts-EGFP after 120 minutes at 37 °C with and without treatment with 100µM MG132. A minimum of 500 cells per condition from 3 biologically independent experiments were counted and two-tailed Student's t-tests were performed comparing the WT yeast without MG132 treatment to WT yeast with MG132 treatment using Prism software. P values were adjusted using two-stage linear step-up procedure of Benjamini, Krieger and Yekutieli with a Q of 5%. Adjusted P value for nuclear no MG132 vs. +MG132 is 0.0035 and cytoplasmic no MG132 vs. +MG132 is 0.0011. Data are shown as mean values ± S.E.M. **(b)** Representative Structured Illumination super-resolution microscopy images taken of cells expressing EGFP-VHL after 2 hr at 37 °C with DMSO (left) or with 100µM MG132 (right) treatment. VHL is shown in green, nuclear pores in gold, and Hoechst counterstain in blue. Scale bars are 1µm. Numerical source data are available in source data.

Extended Data Fig. 3 INQ-JUNQ homing does not occur at the LINC, nucleolus, or involve FG repeats of the nuclear pore central channel.

(a) Graph of the X-Y positions of the INQ and JUNQ compartments by particle tracking of inclusions from cell shown in Figure 2a over the time course of the experiment. **(b)** Representative confocal image taken of cells co-expressing NLS-EGFP-VHL and NES-DsRed-VHL after 2 hr at 37 °C and treated with 100µM MG132. NLS-fusion proteins are shown in green, NES-fusion proteins in purple, nuclear pores in gold, and Hoechst counterstain in blue. Scale bar is 1µm. **(c)** Representative confocal fluorescence microscopy images taken of cells co-expressing NLS-EGFP-LuciTs and NES-DsRed-LuciTs (left) after 2 hr at 37 °C and treated with 100µM MG132. NLS-LuciTs is shown in green, NES-LuciTs in purple, nucleolus (Nsr1) in gold and Hoechst counterstain in blue. (right) Line intensity profile showing distance between nucleolus and homed INQ/JUNQ. Scale bars are 1µm. **(d)** (left) schematic of Mps3 component of LINC complex linking inner and outer nuclear membranes. (right) Representative widefield fluorescence microscopy images taken of cells co-expressing endogenously tagged Mps3-EGFP and NES-DsRed-LuciTs after 120 minutes at 37 °C with and without treatment with 100µM MG132. White arrowheads indicate locations of Mps3 puncta while yellow arrowheads indicate NES-LuciTs puncta. Scale bars are 1µm. **(e)** WT (top) and *nupΔFG* (bottom) cells co-expressing NLS-LuciTs and NES-LuciTs were shifted to 37 °C and monitored by live cell time-lapse fluorescence microscopy for the times shown. Scale bars are 1µm.

Extended Data Fig. 4 Detailed representation of the cryo-SXT workflow and interactions between mitochondria and cytoplasmic PQC compartments.

(a) Optical path through the specimen. Key: COL, cryogenic objective lens; SS, specimen stage; SP, specimen port; MG, motorized goniometer; CIM, cryogenic immersion fluid; CCL, low magnification cryogenic objective; CS, cryogenic specimen; CIE, cryogenic imaging environment; AP, adapter port; AW, a heated, angled anti-reflection window. **(b)** Alignment of fluorescence and soft x-ray tomographic data using fiducial markers. **(c)** A representative confocal image of the spatial relationship between the INQ and nucleolus. NLS-LuciTs (INQ) is shown in green, nucleolus in gold, and Hoechst counterstain in blue. Scale bar is 1µm. **(d)** The interaction between mitochondria and cytoplasmic inclusions is also seen by fluorescence confocal microscopy in a representative image of a cell co-expressing mito-GFP and NES-RFP-LuciTs. NES-LuciTs is shown in purple, mitochondria in cyan, and Hoechst counterstain in blue. Scale bar is 1µm. **(e)** Representative confocal fluorescence microscopy images taken of WT, fission mutants (*dnm1Δ* and *fis1Δ*) and fusion mutant

(*fzo1Δ* and *ugo1Δ*) cells expressing mito-GFP and NES-DsRed-LuciTs after 120 minutes at 37 °C and treated with 100μM MG132. Mito-GFP is shown in cyan, NES-LuciTs in purple, and Hoechst counterstain in blue. Scale bars are 1μm.

Extended Data Fig. 5 NVJ -mediated clearance of misfolded proteins.

(a) Endogenously tagged Nvj1-GFP yeast expressing Ubc9Ts-ChFP were shifted to 37 °C and monitored by live cell time-lapse fluorescence microscopy for the times shown. White arrowheads indicate locations of Nvj1 puncta while yellow arrowheads indicate Ubc9Ts-ChFP puncta. Scale bar is 1μm. **(b)** WT (top) and *nvj1*Δ (bottom) cells co-expressing NLS-LuciTs and NES-LuciTs were treated with 100μM MG132 and shifted to 37 °C for 30 mins to preform inclusions. Cells were then placed in media containing 50mg/ml cycloheximide (CHX) and 100μM MG132 at 37 °C and monitored by live cell time-lapse fluorescence microscopy for the times shown. Scale bars are 1μm. (c,d) Quantitation of the percentage of cells containing cytoplasmic inclusions in WT, *nvj1Δ*, and *vac8Δ* yeast co-expressing NLS-EGFP-LuciTs **(c)** and NES-DsRed-LuciTs **(d)** after 2 hr at 37 °C with and without treatment with 100μM MG132. Data are presented as mean values +/- SEM. Numerical source data are available in source data.

Extended Data Fig. 6 ESCRT involvement in the clearance of misfolded proteins.

(a) Representative confocal images of WT yeast co-expressing Chm7-EGFP and either NLS-EGFP-LuciTs (left) or NES-DsRed-LuciTs (right) after 120 minutes at 37 °C and treated with 100μM MG132. Chm7 is shown in teal and remains diffuse throughout the cell, NLS-EGFP-LuciTs in green, NES-DsRed-LuciTs in purple, nuclear pores in gold and Hoechst counterstain in blue. Scale bar is 1μm. **(b)** Representative confocal images of WT and *vps23Δ*, *vps34Δ*, and *vps15Δ* yeast co-expressing NLS-EGFP-LuciTs and NES-DsRed-LuciTs after 2 hr at 37 °C and treated with 100μM MG132. NLS-EGFP-LuciTs is shown in green, NES-DsRed-LuciTs in purple, nuclear pores in gold, and Hoechst counterstain in blue. Insets show the budding INQ encapsulated by nuclear pores. Scale bars are 1μm. Same data as shown in Fig. 6c, but with the green channel separated to clearly detail the colocalization with the cytoplasmic protein.

Extended Data Fig. 7 Vacuole-mediated clearance of INQ and JUNQ.

Representative images of WT cells expressing NES-2xKeima-LuciTs after 2 hr incubation at 37 °C with 100μM MG132. Over time, fluorescence is seen with excitation in the 558 nm channel indicating the NLS-LuciTs has encountered an acidic environment. Insets show the transition from green to red and a structure leaving the inclusion that is fully red. Scale bars on large images are 5 mm. Scale bars on magnifications are 1 μm. Same data shown in Fig. 7d, but with more time points and a larger field of view in the images. Scale bars on large images are 5 μm. Scale bars on magnifications are 1 μm. **(b)** WT cells expressing NES-2xKeima-LuciTs after 85 min incubation at 37 °C with 100μM MG132. **(c)** Longer exposure of the blot shown in Fig. 7f to highlight the difference in the number and pattern of the EGFP bands in the WT vs *pep4Δ* cells. **(d)** Levels of EGFP at time 0 were measured from Quantitative Western blots such as those shown in Fig. 7e, f (mean ± S.E.M. from three biologically independent experiments). WT and *pep4Δ* yeast were compared using a two-tailed paired Student's t-test without reaching statistical significance. **(e)** WT yeast expressing NLS-EGFP-LuciTs were treated with 8μM of FM4-64 and incubated for 2hr at 37 °C with 100μM MG132. Cells were imaged every 30 sec for 90 mins. Scale bar is 1μm. Same data shown in Fig. 7h, but only WT and with more timepoints during the entry into the vacuole. Source numerical data and unprocessed blots are available in source data.

Supplementary information

Reporting Summary

Supplementary Video 1

Live-cell time-lapse fluorescence microscopy of JUNQ and INQ formation. WT cells expressing NLS-LuciTs (left) or NES-LuciTs (right) at 37 °C, treated with 100 µM MG132. Same data shown in stills in Fig. 1c(left) and Fig. 1d (right).

Supplementary Video 2

Dynamic representation of the 3D reconstructions of SR data: shown in Fig. 1e (left) and Fig. 1g (right). Videos were created in Volocity.

Supplementary Video 3

Dynamic representation of the 3D reconstructions of SR data: shown in Fig. 2a (left) and Fig. 2b (right). Videos were created in Volocity.

Supplementary Video 4

Live-cell time-lapse fluorescence microscopy data shown in Fig. 3a.

Supplementary Video 5

Dynamic representation of data shown in Fig. 3b.

Supplementary Video 6

Dynamic representation of the 3D reconstruction of data shown in Fig. 3c. Video was created in Volocity.

Supplementary Video 7

Dynamic representation of the 3D reconstruction shown in Fig. 4c. Video was created in Amira.

Supplementary Video 8

Dynamic representation of the 3D reconstruction shown in Fig. 4d,f. Video was created in Amira.

Supplementary Video 9

Live-cell time-lapse fluorescence microscopy of the data shown in Fig. 5a.

Supplementary Video 10

Dynamic representation of the 3D reconstruction of the data shown in Fig. 5c. Video was created in Volocity.

Supplementary Video 11

Dynamic representation of the 3D reconstruction of the data shown in Fig. 5b. Video was created in Volocity.

Supplementary Video 12

Live-cell time-lapse fluorescence microscopy of the data shown in Fig. 5f shown at 5 frames s^{-1}.

Supplementary Video 13

Live-cell time-lapse fluorescence microscopy of the data shown in Fig. 5f shown at 2 frames s^{-1}.

Supplementary Video 14

Live-cell time-lapse fluorescence microscopy of the data shown in Fig. 5f shown at 2 frames s^{-1}. Only the 488 nm channel is shown in greyscale.

Supplementary Video 15
Dynamic representation of the 3D reconstruction of the data shown in Fig. 5e. Video was created in Volocity.

Supplementary Video 16
Live-cell time-lapse fluorescence microscopy of WT cell data shown in Fig. 5h.

Supplementary Video 17
Live-cell time-lapse fluorescence microscopy of *nvj1*Δ cell data shown in Fig. 5h.

Supplementary Video 18
Live-cell time-lapse fluorescence microscopy of *vps4*Δ cell data shown in Fig. 5h.

Supplementary Table 1
Supplementary tables of yeast strains and plasmids.

Source data

Source Data Fig. 2
Statistical source data.

Source Data Fig. 2
Unprocessed western blots.

Source Data Fig. 3
Numerical source data.

Source Data Fig. 5
Statistical source data.

Source Data Fig. 6
Statistical source data.

Source Data Fig. 7
Statistical source data.

Source Data Fig. 7
Unprocessed western blots.

Source Data Extended Data Fig./Table 1
Unprocessed western blots.

Source Data Extended Data Fig./Table 2
Statistical source data.

Source Data Extended Data Fig./Table 5
Statistical source data.

Source Data Extended Data Fig./Table 7
Statistical source data.

Rights and permissions